High Altitude Star Formation and the Superbubble Connection

By

Gurvarinder

A thesis submitted to Macquarie University

for the degree of Master of Research

Department of Physics and Astronomy

Submission date: 27 October 2018

Typeset in LaTeX 2_ε.

Except where acknowledged in the customary manner, the material presented in this thesis is, to the best of my knowledge, original and has not been submitted in whole or part for a degree in any university.

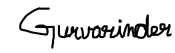

Gurvarinder

Acknowledgements

I owe the ardent gratitude towards my worthy supervisor, Dr Joanne Dawson, for placing her trust in me and providing me with this opportunity to work with her. I am thankful to her for providing a positive learning environment, for her insightful guidance, being patient and helping me improve.

I would also like to thank my co-supervisor, Dr Cormac Purcell, for taking time out of his busy schedule to guide me.

A word of thanks to Anita, Chika and all the members of the radio group for providing a friendly atmosphere and encouraging me throughout this work.

I have to thank my parents, Parminderjeet Singh and Jaswinder Kaur, as well as my brother, Rupinder Singh, for their love, encouragement and moral support. Thank you for giving me the strength to chase my dreams.

Abstract

The thesis is a case study of "Carina Flare" (GSH 287+04–17) – a supershell with significant quantities of associated molecular gas. Since prior studies of the supershell provide substantial evidence of the Galactic Plane blowout, with the highest associated molecular cloud detected $\sim$ 400 pc above the Galactic midplane, it serves as a perfect candidate to investigate the extent of star formation in a small sample of high-altitude clouds. We probe the selected molecular clouds lining the walls of this superstructure using the carbon monosulfide ($J = 1 \rightarrow 0$) rotational transition as a tracer of dense gas clumps. Virial analysis of the detected dense clumps tentatively suggests that most of them may be gravitationally bound and possess a significant potential to collapse to stellar cores. We use the classification scheme for young stellar objects (YSOs) devised by Koenig et al. (2014) combining *WISE* and *2MASS* near and mid-infrared colors and magnitudes to locate YSOs associated with the molecular clouds and investigate their distribution with respect to CS clumps. The close association between the dense gas and YSOs provides substantial evidence in support of on-going star formation activity in the Carina Flare molecular clouds.

Contents

List of Figures

1

Introduction

1.1 Scientific Motivation

The majority of active sites of ongoing star formation in the Milky Way galaxy are confined to a scale height of $\sim$ 50 pc [3] inside the high-density spiral arms, corresponding roughly to the scale height of the molecular thin disk [4]; however, there is increasing observational evidence for star-formation associated with high altitude ($z \gtrsim 200$ pc) molecular clouds [e.g. 5, 6]. A large-scale, methodical study of high altitude molecular clouds (especially the clouds formed in supershells or transported by supernova-driven fountains) and their associated star-formation may provide significant insights into questions related to galaxy evolution and the disk-halo interaction, for instance, the origin of young stars in the Galactic Halo.

Following this path, the principal goal of this project was to conduct a detailed analysis of past, present and future star formation activity in high altitude molecular clouds associated with the "Carina Flare" supershell (GSH 287+04−17). Prior studies of the supershell provide substantial evidence of a Galactic chimney-like structure with associated molecular clouds distributed along its inner boundary (Dawson et al. 2008b catalogued 156 ^{12}CO and 60 ^{13}CO clouds associated with the shell), the highest of these at an altitude of $\sim$ 400 pc above the Galactic midplane [7–10]. Consequently, this superstructure presents an ideal opportunity to study star formation activity at the disk-halo interface, far outside where typical star formation happens.

1.2 Outline

The objective of this 10-month project is twofold:

1. to identify dense clumps that may possess the potential to form stars, and

2. to locate existing young stellar objects,

both of these associated with high altitude molecular clouds in a known supershell, the Carina Flare (GSH 287+04−17). Since the direct detection of neutral molecular hydrogen is generally not possible, we use Carbon monosulfide (CS) as the tracer molecule to detect potential dense star-forming clumps. We have used the Australia Telescope Compact Array (as six single dishes) to observe a select few molecular clouds using the $J = 1 \rightarrow 0$ rotational transition of CS, and gauged their probability to collapse into stellar cores by calculating the virial parameter for each detected clump. This analysis may provide crucial insight into the future star formation activity associated with the supershell.

On the other hand, the presence of young stellar objects (YSOs) in the target area enables us to ascertain the amount of recent star formation. To track down YSOs in and around the molecular clouds, we apply the classification scheme devised by Koenig et al. (2014) [1] combining Wide-field Infrared Survey Explorer (WISE) and Two Micron All-Sky Survey (2MASS) near and mid-infrared colors and magnitudes, on the point source catalogue extracted from the ALLWISE catalogue [11]. Using this photometry scheme, we pinpoint potential Class 1 and Class 2 YSO candidates. We also compare our results with the existing YSO catalogue of Marton et al. (2016) [2]. We can fit the spectral energy distributions (SED) of the candidate YSOs with multi-wavelength data utilising the SED fitting tool of Robitaille et al. (2007) [12]. These SEDs can be used to estimate stellar parameters, for instance, bolometric luminosities.

This thesis is organised into six chapters. Chapter 1 introduces the "Carina Flare" supershell, CS as a dense gas tracer, the relevant radiative transfer and level population equations, and young stellar objects. Chapter 2 provides the details of the data used. Chapter 3 presents the YSO classification scheme based on WISE colors. In chapter 4 we report the CS observations of the molecular clouds. The results presented in Chapter 3 and 4 are discussed in Chapter 5, followed by conclusions and possible future work in Chapter 6.

1.3 Cosmic Bubbles

The Interstellar Medium (ISM) is the name given to the matter and radiation between the stars, and is an essential component in the complex framework of the Galaxy. It has long been known that the interstellar medium is not a latent reservoir of matter but is a dynamic non-homogeneous entity that plays a crucial role not only in the life cycle of stars but also drives the evolution of the Galaxy. Correspondingly, the stars as well as the stellar remnants, actively influence the composition and the physical properties of the surrounding ISM [13]. Massive stars inject mechanical energy into the

ambient medium via stellar radiation, stellar winds (throughout their life) and eventually supernova explosions at the end of their evolutionary life cycle (especially core-collapse supernovae). Such energetic interactions sweep up and compress the ambient medium into shell-type structures over a timescale of millions of years, and based on the concentration as well as the evolutionary status of the energy source these structures can be broadly categorised into three distinct classes namely bubbles, superbubbles (or supershells) and supergiant shells (SGS) [14]. Of these, supershells and supergiant shells are megastructures of up to 1 kpc in diameter, and are a product of multiple supernova explosions concentrated in space and time (for example, in connection with OB associations). They are also often related to episodes of "Galactic blowout". Evidence for the existence of large-scale structures extending vertically above the galactic plane, reaching heights of 200 pc to 1kpc, first came from the observations of the atomic gas distribution in the Galaxy. Heiles (1984) neologized the name "worms" for these structures [15]. These vertical structures turned out to be the walls of supershells that had broken out of the Disk – sometimes also known as chimneys – puncturing the galactic disk, and replenishing the Galactic Halo with hot gas, dust and kinetic energy. Here in the chimney walls, the dust may act as a catalyst for the formation of molecules as well as a shield against Ultraviolet radiation, providing favourable conditions for molecular cloud and star formation (identical to the mechanisms in the Galactic Plane). Dawson et al. (2011a, 2013a) [10, 16] provide substantial observational evidence in support of enhanced molecularization in the walls of supershells and supergiant shells in the Milky Way and Large Magellanic Clouds.

1.3.1 Carina Flare Supershell

In this research project, we study star-formation in high-altitude clouds associated with the "Carina Flare" supershell, a Galactic chimney whose highest regions extend as to the Disk-Halo interface ($z \sim 500$ pc). This superstructure, discovered using the NANTEN 4 m telescope (Chile) in 2.6 mm CO ($J = 1 \longrightarrow 0$) emission line data, is located on the near side of the Carina arm of the Galaxy at an approximate distance of 2.6 kpc [7, 8]. Extensive study of the shell's multiphase ISM in the HI 21 cm line with the Parkes 64 m telescope reveals a gently expanding HI supershell with an approximately elliptically-shaped cavity (eccentricity ~ 0.8). This almost egg-shaped structure, circumscribed by a giant molecular cloud from below, partially curved walls on the left and right and a molecular structure at a high altitude of ~ 400 pc, has a discontinuity at the top left-edge in the form of a ~ 200 pc wide gap [8], evidencing its Galactic Plane blowout.

A plausible scenario for the origin of this supershell, suggested by Fukui et al. (1999, [7]) and

later corrected by Dawson et al. (2008a, [8]) is a chain of several supernova explosions from a cluster of ~ 30 OB stars over a timescale of $\sim 0.8 \times 10^7$ years corresponding to an energy input of $\sim 5 \times 10^5$ erg. To support their theory, the authors report the detection of about 50 late B stars (B4 - B9) in the immediate neighbourhood of the supershell, which may represent the parent OB cluster [7]. In their scenario, the resulting blast waves created a cavity of tenuous hot gas while simultaneously compressing the ambient medium into a thick layer of relatively cold neutral gas, where the next generation of star-formation could be triggered. Indeed, Dawson et al. (2011a) report an enhanced molecular gas fraction within the volume of space affected by the shell, supporting a scenario in which much of the associated molecular material was newly formed from the accumulated atomic medium.

The comoving molecular cloud complex has been extensively studied and catalogued using the $J = 1 \rightarrow 0$ rotational line of ^{12}CO and its isotopologue ^{13}CO by Dawson et al. (2008b, [9]). The analysis conducted on the catalogued clouds using the CO data reveal the structures to be highly sub-virialised, suggesting that they are in general not globally gravitationally bound. We will repeat this analysis on a small sample of clumps detected in the CS $J = 1 \rightarrow 0$ rotational line, to further comment on their gravitational stability.

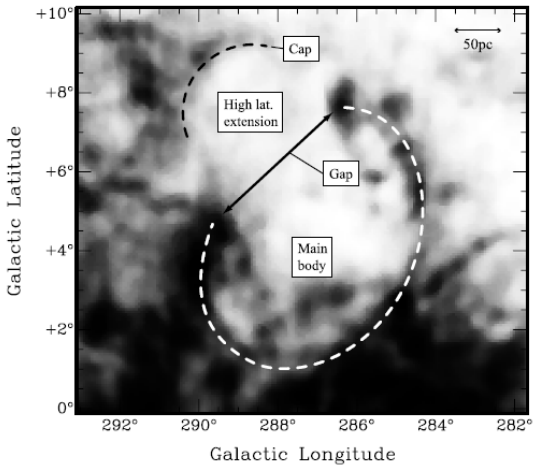

Figure 1.1: Single HI velocity channel map illustrating the main morphological features of the Carina Flare. Adopted from Dawson et al. 2008a

Another interesting morphological feature associated with the supershell, visible in HI and reported by Dawson et al. (2008a), are pillar-like structures, most of them pointing radially inwards towards the interior of the supershell. Follow-up study of these pillar-like structures, for instance, Cloud G288.27+5.60 using HI, ^{12}CO and its isotopologues reveal the existence of dense molecular clumps at their tips, enshrouded by a layer of diffuse gas that extends to form a tail-like structure; hence the name head-tail clouds [17]. These structures are strongly suggestive of a shock front or outflow interacting with pre-existing molecular gas – either gas that was present from before the supershell's formation, or that was formed earlier in its history and re-shaped by later supernova explosions.

Since the majority of the supershells discovered in the Milky Way Galaxy do not exhibit such clear evidence for associated molecular gas, the "Carina Flare" supershell provides a rare opportunity to

study supershell-triggered star-formation activity at high altitudes.

1.3.2 Star formation in the Carina Flare - Current Evidence

Earlier studies of the "Carina Flare" supershell have provided substantial evidence of recent and ongoing star-formation within at least one of the associated molecular clouds. Dawson et al. (2011b) reports a bright, massive and young star-forming region in the cloud G285.90+4.53 [8] at a distance of $z \sim 200$ pc above the Galactic midplane. The cloud is observed in ^{12}CO, ^{13}CO and C^{18}O transition lines with two ^{13}CO emission peaks centred at $(l, b) = (285.91°, 4.52°)$ and $(l, b) = (285.90°, 4.57°)$ that coincide with the ^{18}CO detections. Recent and ongoing star formation activity in the cloud G285.90+4.53 is evidenced by the detection of 2MASS cluster DBSB 49 [18] (an open cluster with estimated age of 2.1 ± 0.3 Myr and home to a massive star of spectral type B0V [19]) and two IRAS young stellar object (YSO) candidates (IRAS 10489-5403 and IRAS 10492-5403) [17].

In addition to the analysis of the molecular clouds associated with the supershell, Dawson et al. (2011a) also present a handful of *IRAS* YSO candidates positionally coincident with several of the clouds, suggesting the possibility that star formation is being triggered as a direct consequence of the interaction between the supershell and the ISM [10]. However, the YSO selection criteria were simplistic, the *IRAS* resolution poor, and no convincing sources were detected in the highest latitude portions of the shell ($b \gtrsim 6°$). Nevertheless, this preliminary work is encouraging, and suggests that more modern IR datasets may yield improved results. In this project, we use the *ALLWISE* source catalogue (because it covers the whole sky and is 100 times more sensitive than *IRAS* [20]) to identify YSO candidates associated with the molecular clouds in the supershell.

1.4 Interstellar Hydrogen and Carbon Monosulfide

1.4.1 Hydrogen in the ISM

Hydrogen is the most abundant element in interstellar space; therefore the state of hydrogen is used to describe the phase of the ISM – atomic, ionised or molecular. The different phases of interstellar hydrogen were first predicted, and then detected, as theoretical physics and observational techniques developed rapidly over time. In this section, we briefly discuss the different probes employed to detect different phases of hydrogen in the ISM.

Atomic Hydrogen (HI): H.C. van de Hulst, the student of Dutch astronomer Jan Oort, predicted

in 1944 that neutral hydrogen could emit at 21 cm radio wavelengths via the hyperfine transition of its ground state [21]. This line emission (or absorption) occurs between two hyperfine levels of $1^2S_{\frac{1}{2}}$ in the ground state of hydrogen. These two states with opposing electron/proton spin configurations, as seen in Figure 1.2, have small energy difference which corresponds to the frequency $\nu_{10} = 1420.405\,752\,\text{MHz}$ ($\sim 21\,\text{cm}$).

Ionised Hydrogen (HII): The ionised component of the ISM is seen both confined to discrete regions around hot stars and also throughout the ISM at low surface brightness, with the amount of ionisation increasing towards the centre of the galaxy [22]. The study of the distribution, kinematics and other physical properties of the ionic hydrogen phase that permeates the galactic plane and halo is generally done using the Hα recombination line and radio free-free emission [23].

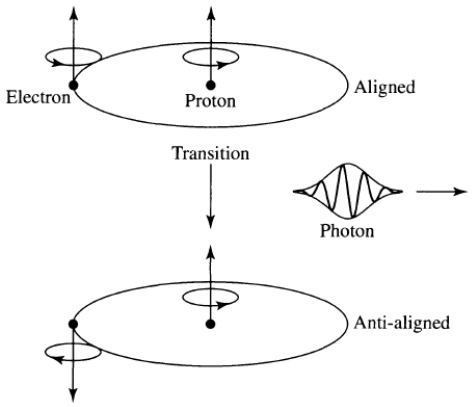

Figure 1.2: The figure illustrates the spin configuration in the two ground state hyperfine levels (the figure is adopted from An Introduction to Modern Astrophysics by Carroll & Ostlie)

Molecular Hydrogen (H_2): Moving forward to molecular hydrogen, the principal chemical component of giant molecular clouds; though it has resonance absorption lines in far-UV and shorter wavelength regimes, it radiates ineffectively at temperatures typical of cold, unexcited ISM. This behaviour can be explained easily through the analysis of the structure and the energy levels of H_2. Firstly, molecular hydrogen is a homonuclear molecule possessing no permanent dipole moment; as a result, the ground-electronic state rotational or vibrational transitions in the electric, as well as the magnetic dipole, are forbidden [24]. Even the detection of electric quadruple rotational and vibrational transitions is difficult owing to their low probability. Secondly, the ground state of molecular hydrogen has no hyperfine structure, so the observation of an emission line analogous to 21 cm radio line of atomic hydrogen is impossible. Finally, the small moment of inertia of H_2 results in widely spaced rotational energy levels – the first excited rotational state lies 518 K above ground. As a consequence, excitations are extremely rare in gas at the low temperatures typical of molecular clouds, where all observed star formation takes place [25]. All the above reasons lead to the conclusion that the most abundant molecule in the ISM, playing a pivotal role in diverse physical and chemical phenomena, is virtually invisible to direct observation.

1.4.2 Tracers of Interstellar H_2

Molecular clouds are the sites of most of the Milky Way's star formation. These clouds have sizes in the range of ~10–100 pc, masses between $\sim 10^4$–$6 \times 10^6 M_\odot$ (though there is no restriction on the upper limit of the total mass) and have mean densities of the order of $100\,\mathrm{cm}^{-3}$. However, owing to their inhomogeneity as well as the impact of external forces, the molecular gas fragments into pockets of high density. These high-density regions include "filaments" (highly elongated structures), "clumps" (typically referring to structures with size scales of ~0.1–1pc) and "cores" (typically referring to structures smaller than ~ 0.1 pc) that may eventually become self-gravitating and collapse to form young stellar objects.

In order to study these phenomena observationally, we must find a way to trace molecular hydrogen in the ISM. This is commonly done by observing co-existing species such as CO, CS and their isotopologues to trace H_2 in molecular clouds and provide information about physical parameters such as column densities, temperatures, gravitational stability, et cetera (provided the abundance ratios of these molecules to the molecular hydrogen are known).

In addition to those mentioned above, in the second half of the twentieth century many molecules, such as OH [26], NH_3 [27], H_2O [28], formaldehyde (CH_2O) [29], et cetera, were discovered in the millimetre, sub-millimetre and microwave wavelength regimes which serve as spectroscopic proxies for molecular hydrogen and can be employed to probe different environments and chemistries. Out of the many molecules that can be used to map molecular hydrogen and investigate the physical parameters of the ambient environment, in the current project we are working with ^{12}CO and its isotopologues ^{13}CO, C^{18}O, as well as CS.

Carbon monoxide (CO)

CO is the next most abundant chemical constituent of molecular clouds after H_2. It is an efficient and widely used tracer molecule as it exhibits an intense rotational spectrum at the low ambient temperatures (~10–20 K) typical of molecular clouds. The discovery of the ubiquitous $J = 1 \rightarrow 0$ rotational transition of ^{12}CO at 2.6 mm [30] (and of its isotopologues) paved the way for the analysis of molecular hydrogen in the ISM. The low rotational transitions ($J < 4$) of CO are a valuable tool to probe the coldest regions in the ISM since these transitions lie 5-22 Kelvin above the ground state. The qualitative and quantitative relationship between CO emission and H_2 has been established by various studies (Liszt 1973; Dickman 1975; Knapp and Jura 1976). Different isotopologues of CO trace different characteristic column densities of H_2. ^{12}CO molecules are ~ 69 × more abundant than ^{13}CO

molecules [31] and the ^{18}CO isotopomer is even less abundant than ^{13}CO. Consequently, ^{13}CO and ^{18}CO have been widely used to observe star-forming clouds and clumps, and are often a better probe than ^{12}CO, which tends to saturate at densities $\geq 10^3$ cm^{-3} [32]. Conversely, ^{12}CO is well-suited to mapping the full extent of a molecular gas cloud, including the more diffuse envelope, but is unable to reliably probe its densest inner regions. The Carina Flare supershell, the target region for this project, has been observed in ^{12}CO (at 115.3 GHz), ^{13}CO (at 110.2 GHz) and C^{18}O (at 109.8 GHz) lines, and the data obtained was employed to calculate the column densities and other physical parameters of the associated molecular clouds [8–10, 17].

1.4.3 Carbon Monosulfide (CS)

Numerous multi-transitional studies have revealed that among the sulphur-bearing species, Carbon monosulfide (CS) is an excellent probe of very dense gas [33]. It has seven transitions ($J = 1 \rightarrow 0$ through $J = 7 \rightarrow 6$) in the millimetre and sub-millimetre regime [34]. Carbon monosulfide is not detected unless the particle densities exceed a threshold value of 3×10^3 cm^{-3} [35]. The critical densities of the first few rotational transitions are summarised in Table 1.1. (To calculate the critical densities in the Table 1.1 the Einstein coefficient A_{ij} were obtained from Splatalogue and the temperature range is, 20 K - 40 K.)

The critical density for excitation of the $J = 1 \rightarrow 0$ line is $\sim 10^4$ cm^{-3}, which is an order of magnitude greater than that of CO [31]. The line also tends to be optically thin, making it a good candidate to observe dense and possibly star-forming regions within molecular clouds, and to estimate their column densities. In this project, to probe regions with densities of the order of $\gtrsim 10^4$ cm^{-3}, we employ the $J = 1 \rightarrow 0$ rotational transition (at 48.990 957 GHz) of Carbon monosulfide.

Table 1.1: Critical Density

CS Transition	Critical density (cm^{-3})
$(J = 1 \rightarrow 0)$	1.74×10^4
$(J = 2 \rightarrow 1)$	1.69×10^5
$(J = 3 \rightarrow 2)$	6.14×10^5

1.5 Physical parameters from molecular line observations

Molecular spectroscopy is a highly useful tool, and can provide information on parameters such as molecular hydrogen column densities, molecular volume densities, molecular isomer and isotopomer ratios, chemical composition, et cetera [36]. Since CS is a dense gas tracer (see section 1.4.3), in this

project we use the CS $J = 1 \rightarrow 0$ transition line observations to derive the molecular column density, that is in turn utilised to calculate the masses of the molecular clumps.

1.5.1 Expression for Molecular column density

In order to convert the measured intensity of a molecular spectral line into information about the mass of emitting material, we begin by deriving the "column density" – the number of molecules per unit area along the line of sight. In this section we present a general mathematical formulation of the molecular column density for a two energy-level system, that is later used in Chapter 4 to derive the physical parameters of the molecular clouds under analysis. This two-level system is assumed to be in thermal equilibrium so that the relative level population follow the Boltzmann distribution.
Ignoring scattering processes, for instance, those involving electrons or dust, the equation of radiative transfer is expressed as follows [36]:

$$\frac{dI_\nu}{ds} = -\kappa_\nu . I_\nu + j_\nu . \tag{1.1}$$

In equation 1.1, s is the path of propagation along the line of sight, I_ν is the specific intensity, κ_ν is the absorption coefficient

$$\kappa_\nu = \frac{h\nu}{4\pi}(n_l B_{lu} - n_u B_{ul})\phi_\nu, \tag{1.2}$$

and $j_\nu \equiv$ is the emission coefficient

$$j_\nu = \frac{h\nu}{4\pi}(A_{ul} n_u). \tag{1.3}$$

The symbols in equation 1.2 and 1.3 are: $h \equiv$ Planck's constant; $l \equiv$ lower transition level; $u \equiv$ upper transition level; $n \equiv$ number density (cm^{-3}) in the upper or lower energy level for a transition with frequency ν; $\phi_\nu \equiv$ line profile function; $A_{ul} \equiv$ spontaneous emission coefficient; B_{ul} and $B_{lu} \equiv$ coefficient of stimulated emission and coefficient of absorption respectively.
Because we generally do not possess knowledge of the propagation path of the measured radiation, the independent variable is changed from the pathlength s to optical depth τ_ν, where the relation between s and τ is

$$d\tau_\nu \equiv \kappa_\nu ds. \tag{1.4}$$

Rearranging the terms in equation 1.2 and using the standard relationship between Einstein coefficients: $g_l B_{lu} = g_u B_{ul}$ and $A_{ul} = \frac{2h\nu^3}{c^2} B_{ul}$ (where g_u and g_l are the degeneracies of the upper and lower level respectively), the absorption coefficient can be written as

$$\kappa_\nu = \frac{c^2}{8\pi\nu^2}\frac{g_u}{g_l} n_l A_{ul} \left(1 - \frac{n_u g_l}{n_l g_u}\right) \phi_\nu. \tag{1.5}$$

Since the purpose of this formulation is to use molecular line observations to calculate molecular column density, we use the definition of the optical depth (eq. 1.4), the expression of the absorption coefficient κ (eq. 1.5), definition of the column density in a given level (in this case the number of molecules in energy level l integrated over a pathlength ds [36]),

$$N_l \equiv \int n_l(s)\, ds, \tag{1.6}$$

the Boltzmann equation of statistical equilibrium, and the definition of spontaneous emission coefficient (for dipole emission) [36]

$$A_{ul} \equiv \frac{64\pi^4\nu^3}{3hc^3}|\mu_{lu}|^2, \tag{1.7}$$

(where $|\mu_{lu}|^2$ is the dipole matrix element) to relate τ_ν to the number of molecules in the lower energy level, N_l:

$$\begin{aligned}\tau_\nu &= \frac{c^2}{8\pi\nu^2}\frac{g_u}{g_l} A_{ul}\phi_\nu \int n_l(s') \left(1 - \frac{g_l}{g_u}\frac{n_u(s')}{n_l(s')}\right) ds' \\ &= \frac{8\pi^3\nu}{3hc}\frac{g_u}{g_l}|\mu_{lu}|^2 N_l \phi_\nu \left(1 - \exp\left(-\frac{h\nu_{ul}}{k_B T_{exc}}\right)\right)\end{aligned} \tag{1.8}$$

$$\int \tau_v dv = \frac{8\pi^3}{3h}\frac{g_u}{g_l} N_l |\mu_{lu}|^2 \left(1 - \exp\left(-\frac{h\nu_{ul}}{k_B T_{exc}}\right)\right). \tag{1.9}$$

To get eq.1.9 from eq.1.8 we change the frequency axis to velocity and integrate over the line profile function, which is defined such that its integral is unity. Rearranging the terms in eq.1.9, the expression for the column density of molecules in the lower transition state is as follows

$$N_l = \frac{3h}{8\pi^3|\mu_{lu}|^2}\frac{g_l}{g_u}\left(1 - \exp\left(-\frac{h\nu_{ul}}{k_B T_{exc}}\right)\right)^{-1} \int \tau_v dv. \tag{1.10}$$

In order to relate the column density in eq. 1.10 to the total molecular column density as measured by the intensity of transition at frequency ν, we assume detailed balance at a constant temperature (excitation temperature T_{exc}) and use the following expression:

$$N_l = N_{Tot}\frac{g_l e^{-E_l/k_B T_{exc}}}{Q_R}, \tag{1.11}$$

where N_{Tot} is the total population of all energy levels in the molecule and Q_R is the rotational partition function of the molecule. Hence, the expression of the total molecular column density is given by:

$$N_{Tot} = \frac{3h}{8\pi^3|\mu_{lu}|^2}\frac{Q_R}{g_u}e^{-E_l/k_BT_{exc}}\left(1-\exp\left(-\frac{h\nu_{ul}}{k_BT_{exc}}\right)\right)^{-1}\int \tau_v dv. \tag{1.12}$$

In this final expression, the unknowns are τ_v and T_{exc}, which we will discuss how to obtain later in this section.

Note that the above formulation has been achieved by calculating the molecular column density of the lower energy level (in a two energy-level system), the same can be done by calculating the molecular column density in the upper energy level. The relevant steps are briefly outlined below.

$$\tau_\nu = \frac{8\pi^3\nu}{3hc}|\mu_{lu}|^2 N_u \phi_\nu \left(\exp\left(\frac{h\nu_{ul}}{k_BT}\right)-1\right) \tag{1.13}$$

Change frequency axis to velocity axis, integrate over line profile function and rearrange the terms.

$$N_u = \frac{3h}{8\pi^3|\mu_{lu}|^2}\left(\exp\left(\frac{h\nu_{ul}}{k_BT}\right)-1\right)^{-1}\int \tau_v dv \tag{1.14}$$

Relate the molecular column density to the total molecular column density (using $N_u = N_{Tot}\frac{g_u e^{E_u/k_BT_{exc}}}{Q_R}$).

$$N_{Tot} = \frac{3h}{8\pi^3|\mu_{lu}|^2}\frac{Q_R}{g_u}e^{E_u/k_BT_{exc}}\left(\exp\left(\frac{h\nu_{ul}}{k_BT}\right)-1\right)^{-1}\int \tau_v dv \tag{1.15}$$

1.5.2 Deriving τ_v From Radio Astronomical Observations

The general solution to the equation of radiative transfer (eq. 1.1) in the case of a single isothermal cloud is given by

$$I_\nu = I_0 e^{-\tau_\nu} + B_\nu(1-e^{-\tau_\nu}), \tag{1.16}$$

where I_0 is the radiation incident on the back of the cloud, B_ν is the source function, which is equal to the Planck function, and all other terms are defined as above. In radio astronomy, specific intensities are commonly recast as temperatures using the Planck equation:

$$I_\nu = B_\nu(T_b) \equiv \frac{2h\nu^3}{c^2}\left(\frac{1}{e^{h\nu/kT_b}-1}\right), \tag{1.17}$$

where T_b is a quantity known as the "brightness temperature" – the temperature a black body would need to have in order to produce the observed intensity I_ν at frequency ν. In the low-energy Rayleigh-Jeans portion of the blackbody curve, I_ν and T_b are linearly related as

$$I_\nu = \frac{2k\nu^2}{c^2}T_b; \tag{1.18}$$

however in the mm-wavelength regime where this assumption does not hold well, we define a "Rayleigh-Jeans equivalent temperature", or "radiation temperature", T_R^*:

$$I_\nu = \frac{2k\nu^2}{c^2}T_R^*; \tag{1.19}$$

$$T_R^* = J_\nu(T_\mathrm{b}) = \frac{h\nu}{k}\frac{1}{(e^{h\nu/kT_\mathrm{b}}-1)}. \tag{1.20}$$

This is the quantity observed by a mm-wavelength radio telescope. We may then relate this observed quantity directly to the optical depth by substituting explicitly for the Planck function in Equation 1.16 and dividing both sides by $2k\nu^2/c^2$. We thus find:

$$T_R^* = J_\nu(T_{bg})e^{-\tau_\nu} + J_\nu(T_\mathrm{ex})\,(1-e^{-\tau_\nu}), \tag{1.21}$$

where T_{bg} is the brightness temperature of the incident radiation on the cloud. Finally, subtracting $J_\nu(T_{bg})$ from both sides will return the line radiation temperature,

$$T_R^*(line) = \left[J_\nu(T_\mathrm{ex}) - J_\nu(T_{bg})\right](1-e^{-\tau_\nu})\,. \tag{1.22}$$

This continuum-subtracted line brightness is the measurable of our CS datacubes; hence, if we have an estimate for the excitation temperature of the relevant levels, we may derive the optical depth across the line profile τ_ν.

1.5.3 Estimating Excitation Temperature, T_{exc}

Since the critical density of the CS $J = 1 \rightarrow 0$ transition is relatively high, we cannot assume that the excitation temperature is as high as the kinetic temperature of the gas. In this project, we therefore use the statistical equilibrium radiative transfer code *RADEX* [37] to estimate a reasonable value for

T_{exc}. RADEX calculates the excitation temperature based on the input physics, such as spectral range, excitation conditions and radiative transfer parameters. The value of the input parameters to calculate the excitation temperature for the CS $J = 1 \rightarrow 0$ is discussed in Chapter 4.

In this section we have derived the expression for molecular column density, required to calculate the LTE mass. The concept as well as the mathematical formulation of the LTE and Virial masses will be discussed in Chapter 4.

1.6 Classification of Young stellar objects

1.6.1 Young Stellar Objects

Young stellar objects (YSOs) are stars in the earliest phases of their life that are still embedded or partially embedded in their birth clouds. They are divided broadly into protostars and pre-main-sequence stars. Since the evolution of a protostar from a dense core is still not fully understood, the empirical classification of the spectral energy distribution (SED; a graph of energy versus frequency or wavelength) serves as a powerful tool to constrain theoretical models [38]. Additional well-known classification methods use spectral index (the slope of $\log_{10} \lambda F_\lambda$ vs $\log_{10} \lambda$ longward of 2 µm) or/and color-color plots to classify a YSO [39]. However, radiation transfer models developed by Whitney et al. (2003a,b and 2004) ([40–42]) suggest that spectral index and color-color plots (when used without SEDs) are not always reliable to correctly determine the evolutionary stage of the YSO [43].

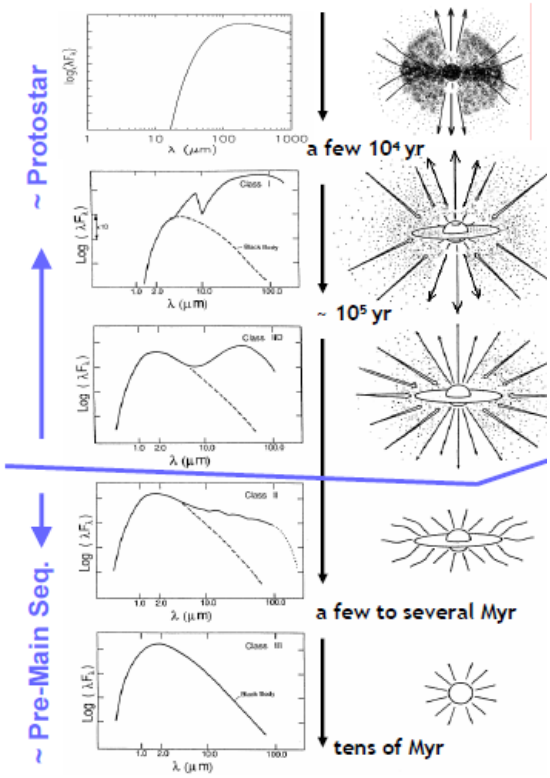

Figure 1.3: Evolution of young stellar objects (Wilking, 1989)

The five evolutionary phases of young stellar objects (low - mass) based on the shape of their SED are:

Class 0: a protostellar core that is completely enshrouded by dust which absorbs the visible and near-infrared radiation from the central source and then re-radiates in the far-infrared and sub-millimetre regimes [44]. The protostellar core is in hydrostatic equilibrium. The spectral energy distribution of a Class 0 source is similar to that of a single-temperature blackbody function with temperature $\leq$ 30 Kelvin [45].

Class I: Characterised by a very broad SED that peaks near 100 µm [40]. The young stellar object is still heavily cloaked with little or no emission from the stellar photosphere. However, due to the presence of a large amount of warm circum-protostellar dust, we can see mid-infrared and near-infrared emission. Almost 50% of the Class 1 sources observed, display atomic emission lines in near-infrared (for example, 10 µm silicate absorption line) but otherwise, the SED is featureless.

Class IIa: an optically thick disk has fully developed, and the phenomenon of disk accretion continues. Stellar winds are strong, leading to the dissipation of the envelope. The 10 µm silicate absorption feature can still present in the SED. The excess emission is in the near-infrared and optical regimes. Wilking (1989) categorises this phase as Class IID. The SED shows a double-peak feature; the first peak corresponds to the emission from the photosphere of the central object in the far-visible/near-infrared regime whereas the second peak arises due to the far-infrared radiation from the cool residual dust envelop.

Class IIb: Molecular hydrogen dissociates leading to the second collapse of the star and re-establishment of hydrostatic equilibrium. The YSO shows surface magnetic activity, reduced rotation rate, and the accretion rate decreases. In this phase, the young stellar object enters the convective-radiative stage of its pre-main-sequence evolution. The gas photosphere and the dust disk combine to produce either a flat spectrum SED if the disk experiences non-viscous accretion (Kenyon & Hartmann, 1957), or a classic T Tauri SED if the disk is undergoing viscous accretion. The SED width is still broader than a single-temperature blackbody function due to the presence of small-quantities of hot dust.

Class III: these sources are post T Tauri stars or naked T Tauri stars. The SED peaks in the visible or near-infrared regime and its shape is similar to that of a single temperature blackbody function. Here the young stellar object is preparing to enter into the main sequence portion of its evolutionary track. The duration of Class III stage is approximately 10^7 yr [46].

From the above-discussed phases, one can summarise that the shape of the SED plays a crucial role in determining the evolutionary state of the young stellar object.

1.6.2 Color-color diagram

The **color-color diagram** is one method used to classify YSOs from the early collapse stage (Class 0) to the remnant disk stage (Class III) (e.g. [47, 48]). **Color** is the difference in brightness (measured in units of apparent magnitude) between two bands. The magnitude of a star is proportional to the log of the flux; therefore, a color is proportional to the ratio of the fluxes. On evaluating the ratio of the flux for the same source, the result is independent of the distance of the star. Hence, the color-color diagram is independent of distances.

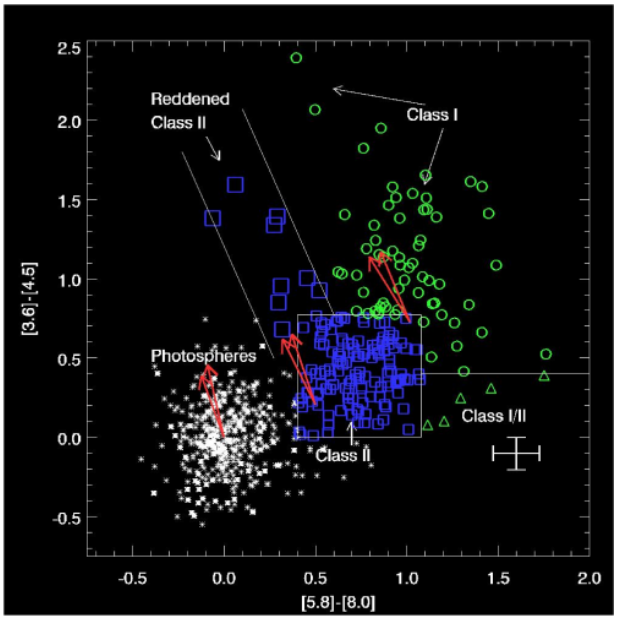

Figure 1.4: Example of a color-color diagram using IRAC colors (Source: http://coolwiki.ipac.caltech.edu/)

Color-color diagrams can be used to: (a) segregate objects of different types; (b) find young stellar objects and (c) estimate their age. Different type of sources occupy distinct and well-defined regions of the color-color diagram and it is possible to some extent to determine the evolutionary nature of the YSO based on its position in the color-color space. For example, the figure shows a color-color diagram made using Infrared Array Camera (IRAC) near infrared colors, which includes only young stellar sources. As is evident from the Figure 1.4, as the YSOs age, they move from right to left on this particular color-color diagram. We employ the YSO classification scheme based on infrared colors and magnitudes devised by Koenig et al. (2014) [1], discussed in Chapter 4, to extract and classify the YSOs in and near the "Carina Flare" supershell.

2

Data

2.1 Data

In this chapter, we briefly outline the salient features of the data sets and the catalogues used in the project.

2.1.1 HI Data

In the current project, HI data (taken from Dawson et al. 2011a [10]) was used exclusively for examining interesting morphological features of the "Carina Flare" supershell, for instance, head-tail clouds. The observations were made using the Australia Telescope Compact Array (ATCA) and covered the region between $283° < l < 292°$ and $1.5° < b < 10.5°$, with ATCA data taken as part of the Southern Galactic Plane Survey (SGPS) [49] used to cover the Galactic Plane region (|b| < 1.0°). The authors combined the synthesis images obtained from the above interferometric data with Parkes 64 - m telescope single-dish data from Galactic All-Sky Survey (GASS) [50, 51]. The spatial and velocity resolutions of the final combined datacube are 2.5 arcminutes and $0.8\,\mathrm{km\,s^{-1}}$. For comprehensive information on the observing strategy as well as data reduction, refer to Dawson et al. (2011a) and McClure-Griffiths et al's (2005) explanatory papers.

2.1.2 NANTEN, MOPRA and APEX CO data

CO data from the NANTEN and Mopra telescopes has already been used to conduct an extensive study of the molecularization in the walls of the Carina Flare supershell by Dawson et al. 2008a, 2008b, 2011a and 2011b ([8–10, 17]). Unpublished APEX telescope data also exists for one cloud, observed as part of the project of Wunsch et al. [52]. In the current project, we use these CO datasets primarily to select regions exhibiting strong detections in ^{13}CO and C^{18}O as targets for followup CS

observations (see below), and also to visualise and contextualise the broader environment in which detected CS clumps reside.

NANTEN data: The NANTEN 4-m telescope in Chile was used to observe the molecular clouds in the GSH287+04−17 region in the ^{12}CO ($J = 1 \rightarrow 0$) and ^{13}CO ($J = 1 \rightarrow 0$) lines at 115.3 GHz and 110.2 GHz, respectively. The CO datasets were originally published by Fukui et al. (1999) [7] and as part of the PhD thesis of Matsunaga (2002), and collected into catalogue form by Dawson et al. (2008b) [9]. The telescope's half power beam width was $\sim 2.6'$ for the ^{12}CO line and $\sim 2.7'$ for the ^{13}CO line, and the clouds of relevance to this study were observed on a $2'$ grid. The raw velocity resolution was 0.1 km s^{-1} [9]. For details on the observing strategy, spatial coverage and data sensitivity refer to the Dawson et al. (2008b) explanatory paper.

Mopra data: Mopra observations of two GSH 287+04-17 clouds were made in the ^{12}CO ($J = 1 \rightarrow 0$), ^{13}CO ($J = 1 \rightarrow 0$) and C^{18}O ($J = 1 \rightarrow 0$) lines at 115.3, 110.2 and 109.8 GHz respectively. For all three lines, the effective beam size (post-gridding) was $\sim$ 35 arcsec, and the raw velocity resolution was $\sim$ 0.1 km s^{-1}. Further technical details related to the instrumentation and observing strategy may be found in Dawson et al. (2011b).

APEX data: APEX observations of one additional GSH 287+04-17 cloud were made in the ^{13}CO ($J = 2 \rightarrow 1$) and C^{18}O ($J = 2 \rightarrow 1$) lines at 115.3, 220.4 and 219.6 GHz. This data was taken as a followup to the work of Wunsch et al. (2012) [52], and is unpublished. The effective half power beam width of this data is $\sim 27''$ and the velocity channel width is 0.66 km s^{-1}. Further details of the observing strategy can be found in the above-cited work.

2.1.3 New ATCA CS data

To further probe the dense regions within the molecular clouds associated with the "Carina Flare" supershell we took new CS ($J = 1 - 0$) line data as the extension to an ongoing StarFISH (**Star** **F**ormation **I**n the **S**outhern **H**emisphere) Survey to map multiple molecular tracers in the Galactic Plane. Observations were performed during ATCA "green time", outside of the primary survey time allocations, and were carried out partly by myself (on 2 March 2018). The survey when complete will cover the majority of the Southern Galactic Plane accessible to the ATCA and will observe the target regions in 12 transitions between $\sim$ 42.5 and 48.9 GHz, using the array as 6 single dishes adopting the

on-the-fly mapping to scan at a rate of 5.02 arcsec s^{-1}, recording data every 6 s. [1]

We scanned in 1 direction only, and took off-source reference spectra every ~ 30 min for bandpass calibration. To ensure that the pointing of individual telescope is accurate to within 5-10 arcsec, a pointing observation (pointing source: 1039-47) was conducted every 1.3 h. A standard calibrator source, 1934-638, was observed once per day for flux calibration. Both the pointing source as well as the standard calibrator are compact, bright extragalactic radio sources. Data reduction was performed by collaborators using a development-version of the full Legacy Project pipeline, which included all standard reduction steps and gridding. For this project we subtracted a residual baseline ripple from the gridded data by fitting polynomials to line-free velocity regions (identified from inspection of cubes and corroborated with CO data). The final spatial and spectral resolutions of the data are ~ 60″ and 0.19 km s^{-1}, with a characteristic per-channel rms noise of ~ 0.02 K. There is some striping due to variable weather conditions.

2.1.4 *ALLWISE* Source catalogue

The Wide-field Infrared Survey Explorer (*WISE* [11]), a NASA medium-class Explorer mission launched on 14 December 2009, surveyed the whole sky simultaneously in four mid-infrared bands centred at 3.4, 4.2, 12 and 22 µm (W1, W2, W3 and W4 respectively). The photometry provided by such infrared catalogues acts as a useful tool to identify and classify young stellar objects, since the location of these bands within the em spectrum coincides with the regime where the cool disks/envelopes of young stars begin to show significant infrared excess emission. The *WISE* photometry minimises the variability between the filters by imaging the four filters simultaneously.

In this project, we opt to work with the *ALLWISE* source catalogue [53], a data product of the *ALLWISE* program that was generated by the combination of data from *WISE* [11] cryogenic and *NEOWISE* [54] post-cryogenic survey phases. It is the most comprehensive sky view in the mid-infrared regime with enhanced photometric sensitivity and accuracy (compared to the earlier 2012 *WISE* All-Sky Data Release). The catalogue contains astrometry and photometry for over 747 million objects detected on the deep *ALLWISE* Atlas intensity images (Image Atlas), and the improved astrometric precision makes it superior to the 2012 *WISE* All-Sky release catalogue [55]. The *ALLWISE* catalogue includes positions, magnitudes, astrometric and photometric uncertainties, flags indicating the reliability and quality of the source characterisations, and associations with the *2MASS* Point and Extended Source Catalogue sources [56] for each source.

[1] The (still unpublished) StarFISH Survey of dense gas tracers in the Southern Galactic Plane. (ATCA)

2.1.5 Why chose *ALLWISE* Source Catalogue over other IR catalogues?

The latest generation of infra-red telescopes, including *Spitzer*, *WISE*, *Akari* and *Herschel*, have all produced new and improved images and source catalogues that have proved to be invaluable tools for YSO identification in the Galaxy. Unfortunately, the Carina Flare region has not been systematically observed by the majority of latest generation surveys, which tend to either be restricted to within a degree or less (in latitude) of the Galactic Plane, or target specific local clouds of interest. At a Galactic Longitude of $283^\circ \lesssim l \lesssim 293^\circ$ and a Galactic Latitude of $3^\circ \lesssim b \lesssim 10^\circ$, the Carina Flare region has been systematically observed only by *WISE* and *Akari*. However, for this project we opted not to utilise the *Akari* point source and bright source catalog, since no YSO identification and classification scheme based on the *Akari* bands has been published. Furthermore, we noticed from comparison with our HI dataset that the *Akari* bright source catalogue (at 65 µm to 160 µm, which would have been the most useful additional wavelengths for our work since they are not covered by *WISE*) tended to primarily detect HI substructure in the walls of the supershell. (We also note that while *Planck* all sky data products cover this region, their low spatial resolution is not well suited to YSO identification.) For this reason we have carried out this initial study using only *ALLWISE* source catalogue.

2.1.6 Marton's YSO catalogue

Marton et al. (2016) analysed the 2MASS and WISE photometry available in the ALLWISE Source Catalogue [53] employing a sophisticated statistical method, the support vector machine (SVM) (in place of color-color and color-magnitude diagrams), to identify and categorise the Young Stellar Object (YSO) candidates. As SVM is a machine learning method, known sources listed in the SIMBAD database were used to train the algorithm. Based on comparison with the existing photometric and spectroscopic catalogues, the SVM selection process boasts a high success rate of > 90 per cent in the identification of YSOs. The catalogue includes 133 980 Class I/II YSOs candidates and is used in the current project to both compare against and supplement the results from the Koenig et al. (2014) color-color classification scheme that we employ in Chapter 4.

3

Identification of Young Stellar Objects

3.1 Introduction

The formation and early evolution of stars occurs inside the densest regions of molecular clouds. Young stellar objects (YSOs) are therefore buried within a significant amount of interstellar dust and gas, and the bulk of their energy is radiated at wavelengths longward of 1 μm. Therefore, observations in the infrared wavelength regime are essential in the investigation of early stellar evolution. The shape of the infrared spectral energy distribution (SED) of a YSO is a robust tool with which to decipher the nature of its circumstellar environment, provided that observations over a wavelength range of $\sim$ 1–100 μm are available. However, useful information can also be obtained from a limited number of near and mid-infrared colors when the available data is plotted on a color-color diagram.

3.2 *ALLWISE* Catalogue Parameters

The *ALLWISE* source catalogue [53] is a data product of the *ALLWISE* program that was generated by combining the data from *WISE* [11] cryogenic and *NEOWISE* [54] post-cryogenic survey phases. It is the most comprehensive sky view in the mid-infrared regime with enhanced photometric sensitivity and accuracy (compared to the earlier 2012 *WISE* All-Sky Data Release). The *ALLWISE* source catalogue [53] which is an improved version of the 2012 *WISE* All-Sky Data Release [55], and has the added advantage that each entry has been positionally cross-correlated with the *2MASS* Point source catalogue [57] and *2MASS* Extended source catalogue. (The search radius used for the *ALLWISE*/*2MASS* PSC was 3″.) Although the *ALLWISE* catalogue contains $\sim$ 79 columns, here we list only the parameters that are actively used in the classification scheme.

[W1]: *WISE* band 1 centred at 3.4 μm.

[W2]: *WISE* band 2 centred at 4.6 µm.

[W3]: *WISE* band 3 centred at 12 µm.

[W4]: *WISE* band 4 centred at 22 µm.

[3.4]: W1 Magnitude measured with profile-fitting photometry.

w1sigmpro: W1 profile-fit photometric measurement uncertainty in magnitude units.

w1snr: W1 profile-fit measurement signal - to - noise ratio.

w1rchi2: Reduced χ^2 of the W1 profile-fit photometry measurement.

[4.6]: W2 Magnitude measured with profile-fitting photometry.

w2sigmpro: W2 profile-fit photometric measurement uncertainty in magnitude units.

w2snr: W2 profile-fit measurement signal - to - noise ratio.

w2rchi2: Reduced χ^2 of the W2 profile-fit photometry measurement.

[12]: W3 Magnitude measured with profile-fitting photometry.

w3sigmpro: W3 profile-fit photometric measurement uncertainty in magnitude units.

w3snr: W3 profile-fit measurement signal - to - noise ratio.

w3rchi2: Reduced χ^2 of the W3 profile-fit photometry measurement.

[22]: W4 Magnitude measured with profile-fitting photometry.

w4sigmpro: W4 profile-fit photometric measurement uncertainty in magnitude units.

w4snr: W4 profile-fit measurement signal - to - noise ratio.

w4rchi2: Reduced χ^2 of the W4 profile-fit photometry measurement.

J: 2MASS *J*-band magnitude of the associated 2MASS PSC source.

H: 2MASS *H*-band magnitude of the associated 2MASS PSC source.

K_s: 2MASS K_s-band magnitude of the associated 2MASS PSC source.

ph_qual flag: The photometric quality flag is a four character flag, one character for each band [W1/W2/W3/W4], that summarises the quality of the profile-fit photometry measurement. The 'A', 'B', 'C', 'U', 'X' and 'Z' are the six characters used to indicate the quality of the photometry in each band.

ext_flag: The Extended source flag is an integer flag. The value of this parameter indicates whether or not the morphology of a source is consistent with that of the *WISE* point spread function, or whether the source is associated with or superimposed on a previously known extended object from the *2MASS* Extended Source Catalog (XSC).

3.3 YSO Classification scheme

In this section, we present the algorithm devised by Koenig et al. (2014) (hereafter: K14), which we employ to identify and classify YSOs in and near the "Carina Flare" supershell (dimensions of the field: $284° \leq l \leq 290°$ and $3° \leq b \leq 10°$). This algorithm is a refined version of the YSO identification and classification scheme published by Koenig et al. (2012) (hereafter: K12), wherein the authors adapted the accepted source classification scheme of Gutermuth et al. (2008, 2009) (based on *Spitzer* colors) to the *WISE* infrared wavebands. Although different types of source occupy overlapping regions in the *WISE* color-color plane [2], K14 use the linear method (a set of linear inequalities to delimit the region occupied by a particular type of source, for instance, Class I YSO) to mitigate contaminants (such as extragalactic sources, PAH features, etc.), identify and classify the YSOs. Since the target region used in this project resides outside the Galactic midplane, following K14, we do not apply any dereddening to the colors of the sources we classify. The scheme described below is employed in the same order as presented in the original publication [1] (with minor modifications).

3.3.1 STEP 1: Extraction of the point source photometry from ALLWISE source catalogue

Since the *ALLWISE* source catalogue is not purely a point source catalogue, we must first select only sources with reliable point source photometry. The only essential requirement we use for the retrieval of point sources is a non-null photometric error in each *WISE* band. This requirement restricts the ph_qual flag only to 'A', 'B', or 'C' in the specific band. The primary goal while constructing the point source catalogue is obtaining reliable photometry in at least three bands. K14 uses criteria based only on the signal-to-noise ratio and profile-fit reduced chi-squared to mitigate contamination. The uncertainty/signal-to-noise/chi-squared criteria used are as follows:

- *WISE* band 1: non-null $w1sigmpro$ and $w1rchi2 < (w1snr - 3)/7$
- *WISE* band 2: non-null $w2sigmpro$
- *WISE* band 3: $w3snr \geq 5$ AND either $w3rchi2 < (w3snr - 8)/8$ or $0.45 < w3rchi2 < 1.15$
- *WISE* band 4: non-null $w4sigmpro$ and $w4rchi2 < (2 \times w4snr - 20)/10$

3.3.2 STEP 2: Removal of astrophysical extragalactic contaminants

The first group of contaminants removed from the point source catalogue (obtained in STEP 1) are unresolved external galaxies. For the removal of these contaminants, K14 make their selection cuts by over plotting the tracks corresponding to theoretical SED templates of different galaxy types (old ['elliptical'], intermediate ['spiral'], and young stellar populations ['irregular'] as well as active galactic nuclei [AGN]) [58] on the color-color diagrams of North polar field sources (that consist mostly of galaxies and Galactic halo stars). In this way, star-forming galaxies and AGN are rejected via the conditions described below.

Removal of star forming galaxies: Sources meeting the following criteria are removed as likely star-forming galaxies (SFG)

$$[4.6] - [12] > 2.3 \tag{3.1}$$

$$[3.4] - [4.6] < 1.0 \tag{3.2}$$

$$[3.4] - [4.6] < 0.46 \times ([4.6] - [12]) - 0.78 \tag{3.3}$$

$$[3.4] > 13.0 \tag{3.4}$$

Removal of AGN's: If a source meets the following set of requirements, it is rejected as a candidate AGN.

either

$$[3.4] > 1.8 \times ([3.4] - [12]) + 4.1 \tag{3.5}$$

$$[3.4] > 13.0 \tag{3.6}$$

or

$$[3.4] > [3.4] - [12] + 11.0 \tag{3.7}$$

3.3.3 STEP 3: Classification of young stellar objects

After the removal of extragalactic contaminants we move towards the identification and classification of the YSOs. This scheme is developed by K14 to follow the observed colors of Taurus region YSOs [59] and transition disk young stars [60].

Extraction of Class 1 YSOs - Candidate protostars: Candidate Class I YSOs are classified as such if they meet the following set of conditions:

$$[4.6] - [12] > 2.0 \tag{3.8}$$

$$[3.4] - [4.6] > -0.46 \times ([4.6] - [12]) + 2.2 \tag{3.9}$$

$$[3.4] - [4.6] > 0.46 \times ([4.6] - [12]) - 0.9 \tag{3.10}$$

$$[4.6] - [12] < 4.5 \tag{3.11}$$

The above identification and classification scheme better matches the division of YSOs based on the SED slope of $\left(a = \dfrac{d \log \lambda F_\lambda}{d \log \lambda}\right)$, when compared to the older scheme published by K12.

Extraction of Class 2 YSOs – Candidate T Tauri stars and Herbig AeBe stars: Out of the remaining sources, Class II YSOs are identified if their colors match the following set of conditions:

$$[3.4] - [4.6] > 0.25 \tag{3.12}$$

$$[3.4] - [4.6] < 0.9 \times ([4.6] - [12]) - 0.25 \tag{3.13}$$

$$[3.4] - [4.6] > -1.5 \times ([4.6] - [12]) + 2.1 \tag{3.14}$$

$$[3.4] - [4.6] > 0.46 \times ([4.6] - [12]) - 0.9 \tag{3.15}$$

$$[4.6] - [12] < 4.5 \tag{3.16}$$

Extraction of YSOs from 2MASS photometry: The following set of conditions are additionally employed to search for YSOs amongst sources possessing *2MASS J H* K_s photometry in the *ALLWISE* catalogue. Deviating from the conditions adopted by K12, K14 use $(H - K_s)$ vs. $(W1 - W2)$ color diagrams. The advantage of these color plots over the $(K_s - W1)$ vs. $(W1 - W2)$ is that it is easier to remove contaminants that may have colors similar to disk excess sources.

$$H - K_s > 0.0 \tag{3.17}$$

$$H - K_s > -1.76 \times ([3.4] - [4.6]) + 0.9 \tag{3.18}$$

$$H - K_s < \frac{0.55}{0.16} \times ([3.4] - [4.6]) - 0.85 \tag{3.19}$$

$$[3.4] \leq 13.0 \tag{3.20}$$

The above selection cuts take special care to avoid erroneously including sources such as AGB stars, Class III/weak disk YSOs, et cetera.

Identification of Transition disks: *WISE* band 4 photometry is employed to identify candidate transition disk objects. The color-color plots constructed by K14 using literature transition disks and Class II sources reveal considerable overlap between the two.

Candidate transition disks are selected from the remaining pool of point sources if following set of conditions are satisfied.

$$[12] - [22] > 1.5 \tag{3.21}$$

$$0.15 < [3.4] - [4.6] < 0.8 \tag{3.22}$$

$$[3.4] - [4.6] > 0.46 \times (4.6 - [12]) - 0.9 \tag{3.23}$$

$$[3.4] \leq 13.0 \tag{3.24}$$

The last two condition are included as an attempt to mitigate the contamination by background galaxies. The selection cuts developed by K14 are unable to separate the bluest transition disks (in *W1 - W2*) color) from the AGB stars and CBe stars without the aid of follow-up spectroscopy and we excluded them from any further analysis.

Extraction of YSOs from previously identified AGN sources: Band 4 photometry is also employed to recover probable protostars from sources previously identified as AGN candidates. Previously classified AGN candidates fulfilling the following conditions are reinstated as YSO candidates:

$$[22] < 5.0 \tag{3.25}$$

$$4.5 < [4.6] - [22] < 8.0 \tag{3.26}$$

$$[3.4] - [4.6] > 1.0 \tag{3.27}$$

$$[12] - [22] > 2.0 \tag{3.28}$$

Elimination of AGB stars and the final list of YSOs: All previously classified YSOs are tested against a set of conditions to eliminate AGB stars. Any type of YSO candidate is rejected from the sample if they meet either:

$$[3.4] < -\frac{10}{3} \times ([3.4] - [4.6]) + 9 \tag{3.29}$$

$$[3.4] < \frac{6}{7} \times ([3.4] - [4.6]) + 5.5 \tag{3.30}$$

or

$$[12] - [22] < 1.9 \tag{3.31}$$

$$[3.4] - [4.6] < [12] - [22] - 0.45 \tag{3.32}$$

3.4 Addition of Marton 2016 YSO Catalogue Sources

Using the K14 YSO classification scheme on the *ALLWISE* sources in our test field, only 22 out of 968 point sources were identified as YSOs, which led us to investigate whether the color cuts might be too restrictive. Recently, Marton et al. (2016) stressed the fact that different types of source have highly

overlapping *WISE* colors, and that commonly-used methods such as color-color and color-magnitude diagrams do not take advantage of the all the available information. The authors instead apply a more sophisticated machine learning algorithm to the entire catalogue [2] and produced a somewhat different (and more forgiving) YSO selection for the entire Milky Way. We used this YSO catalogue to check against our sample, and found that 8 sources were common, and that the Marton et al. catalogue provided 40 additional YSO candidates. These sources should certainly be no *less* reliable than K14, and the fact that 2 sources from Marton's YSO catalogue are coincident with molecular clouds (including the one previously-identified site of SF described in Dawson 2011b [17]) leads us to regard them as reliable. We therefore opt to include both samples in the following analysis.

3.5 Results

The results of the K14 identification and classification scheme are displayed in figure 3.1 along with the YSO candidates from the Marton et al. (2016) YSO catalogue [2] (for $b \gtrsim 3°$). Evident from the image is the fact that very few (~ 6) YSO candidates identified using the K14 scheme match the entries from Marton's YSO catalogue. We note that the at least ~ 10 suspect sources have no clear associations with molecular clouds and lie far from the supershell walls, suggesting they indeed have little to do with recent or ongoing star formation in the Carina Flare. Out of the remaining sources ~ 3 sources lie inside the cavity of the supershell or directly below the molecular cloud (with the young stellar cluster). The distribution of YSOs with respect to dense CS clumps, and the differing performances of the two schemes in our regions of interest are discussed further in Chapter 5.

Figure 3.2 presents a color-color plot of both the Marton's [2] and K14 YSO samples, together with the color cuts (dashed lines) employed by the K14 Classification scheme. The distribution of the candidate YSOs on the color - color plot reveals presence of greater number of Class II sources as compared to Class I sources. Quite few candidate YSOs from the Marton's catalogue spill out of the Class II region delimited by the linear color cuts, indicating non - linear overlap of the *WISE* colors in color space. The K14 classification scheme was able to identify 6 Class I YSO, 13 Class II YSO and 2 Transition disk candidates.

3.6 SEDs

In a attempt to add more information to our near and mid-infrared SEDs (from *ALLWISE* source catalogue) we use an online SED analysing tool – VOSA (Virtual Observatory SED Analyser) [61],

solely to query all the existing catalogues (UV, optical and IR) for constructing more complete SEDs of the candidate YSOs wherever possible in our fields. Figure 3.3 -3.7 presents these SEDs for all YSO candidates in and around detected CS clumps (see following section). It is evident that many of the SEDs are open, due to the lack of data beyond 22 µm (*WISE* band 4). Two out of the 13 sources have IRAS associations, one of which (with coordinates: 285.87°, 4.62°) is classified as a Class I YSO, and is clearly associated with the known massive star-forming region discussed in Dawson et al. (2011b) [17].

In future work, we plan to explore whether these SEDs may be supplemented by other sources of longer wavelength data, and whether useful parameters (such as bolometric luminosity) may be reliably extracted using SED fitting templates, for instance, the Robitaille online SED fitting tool [43].

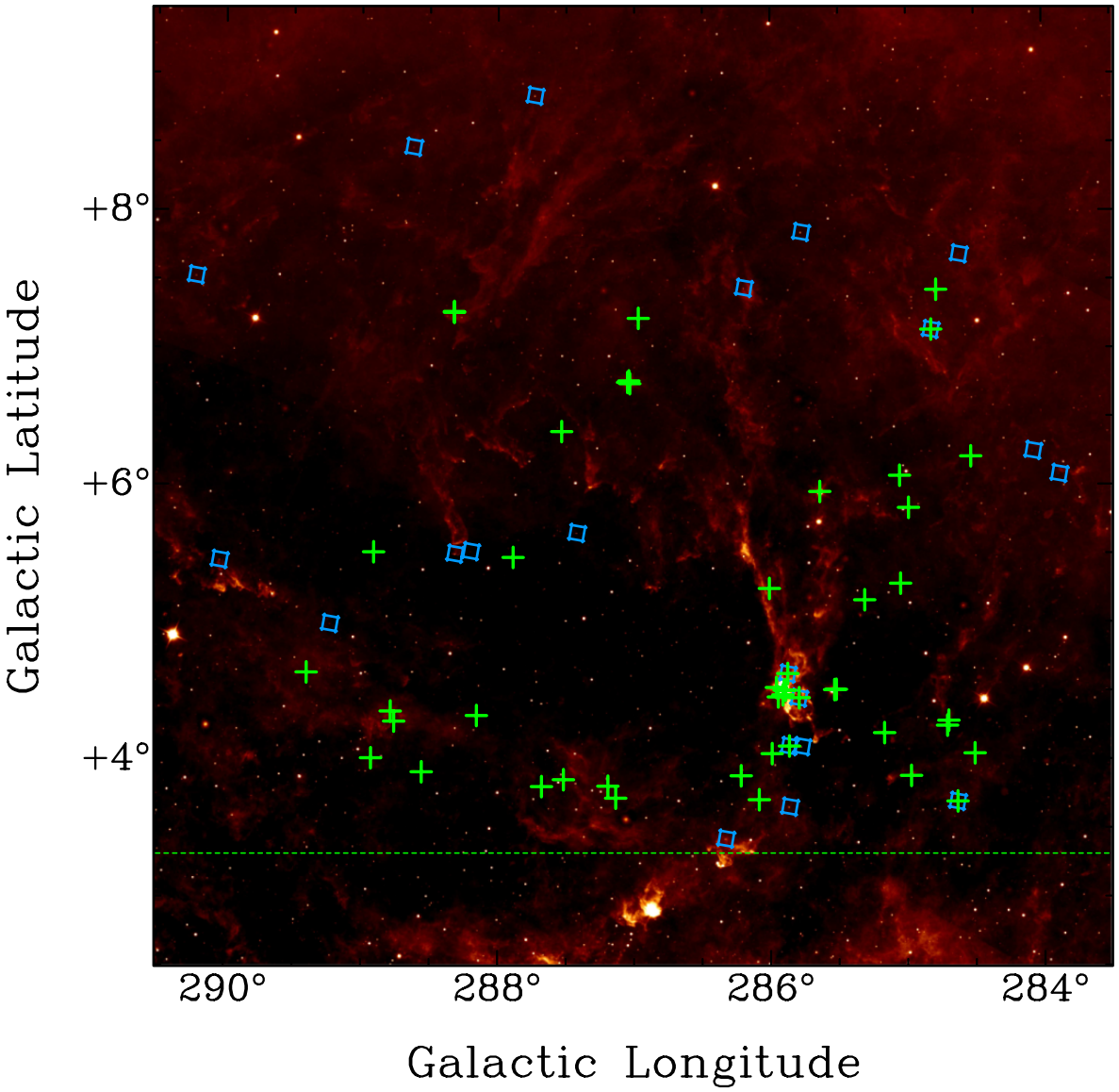

Figure 3.1: YSO candidates identified using the K14 classification scheme (blue squares), and those from the Marton et al. (2016) YSO catalogue (green crosses), in the high-altitude portion of the Carina Flare supershell ($b > 3.2°$; indicated with the green dashed line) overlaid on the *WISE* band 4 (22 µm) image

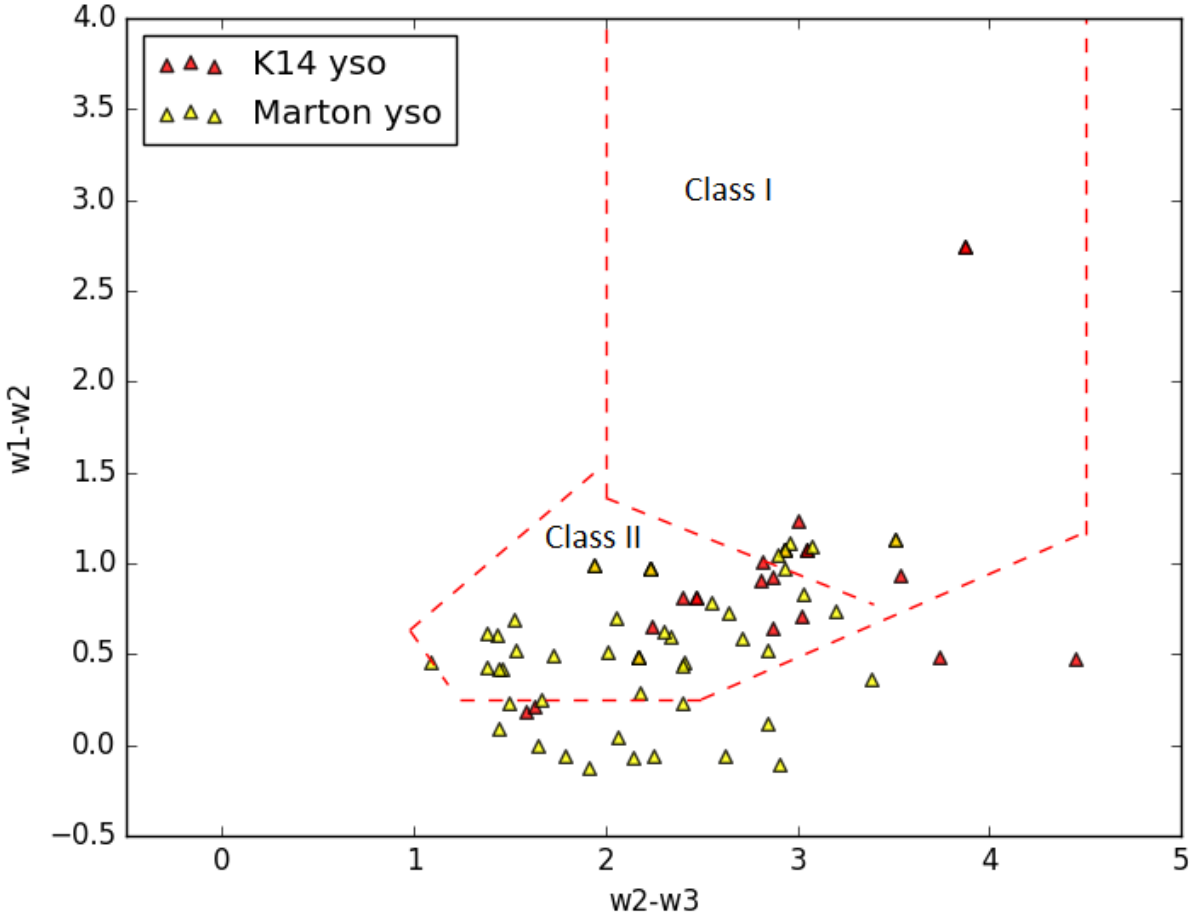

Figure 3.2: *WISE* color-color plot of candidate YSOs obtained by employing the K14 identification and classification scheme [1] on point sources extracted from the *ALLWISE* source catalogue in and near the Carina Flare supershell (red triangles), as well as candidate YSOs from Marton et al.'s YSO catalogue [2] (yellow triangles). The dashed lines show the K14 Class I and Class II divisions. Note that any K14 YSO candidates not enclosed in the boundary delimiting the Class I and Class II regions may belong to another division such as Transition disk candidate. On the other hand, the Marton's Class I/II YSO candidates spilling over the boundaries indicate that the preferred method of classification is based on non - linear methods [2].

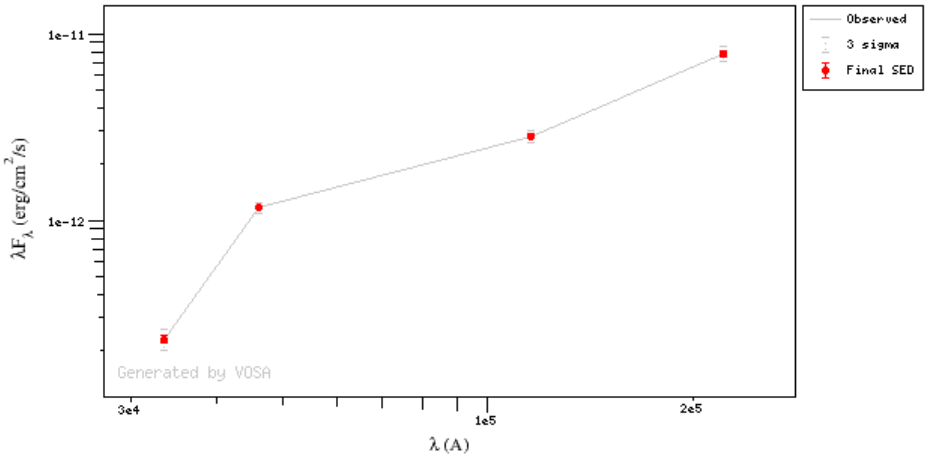

(a) Source coordinates: 288.31°, 5.49°

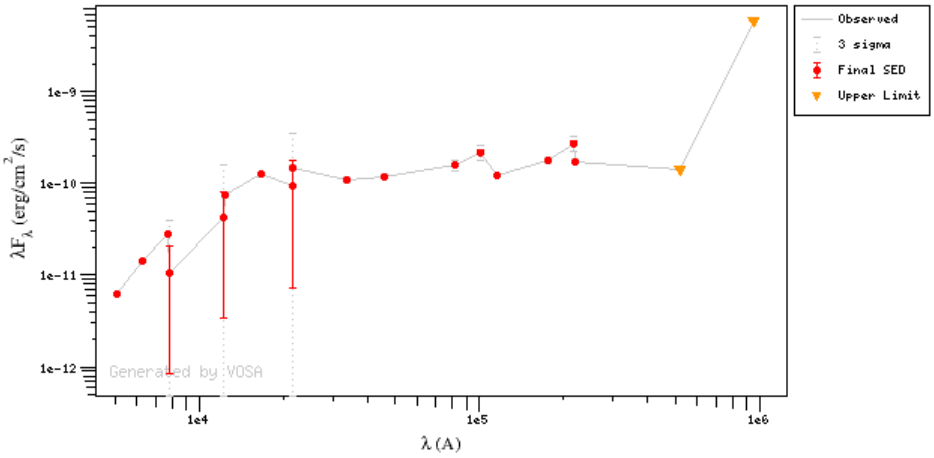

(b) Source coordinates: 285.87°, 4.62°

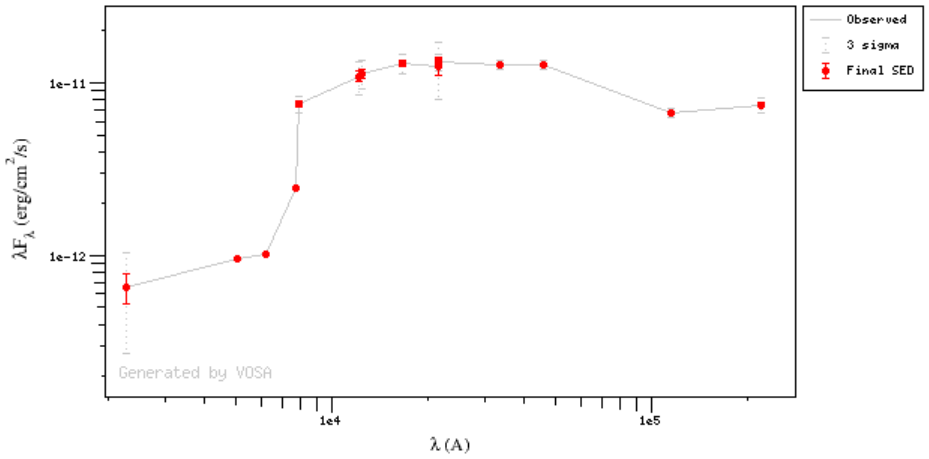

(c) Source coordinates: 285.79°, 4.44°

Figure 3.3: SEDs of the candidate YSOs associated with CS clumps in the Carina Flare supershell and identified using the K14 classification scheme [1].

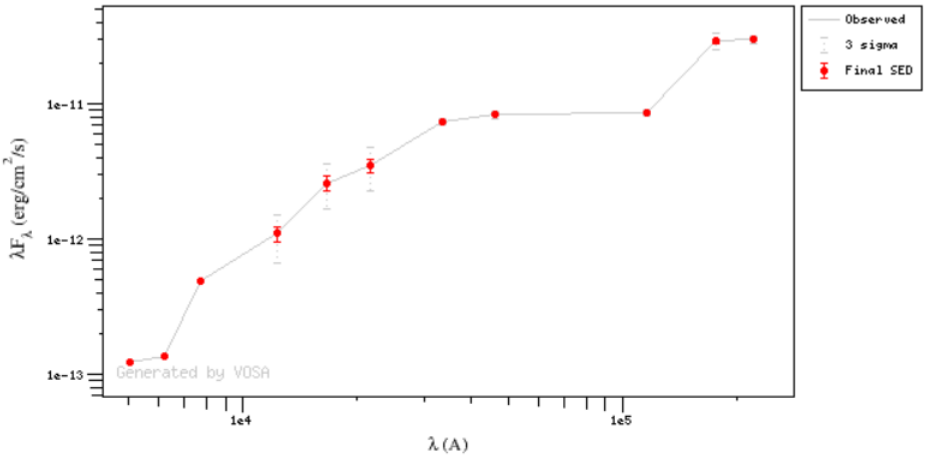

(a) Source coordinates: 286.00°, 5.24°

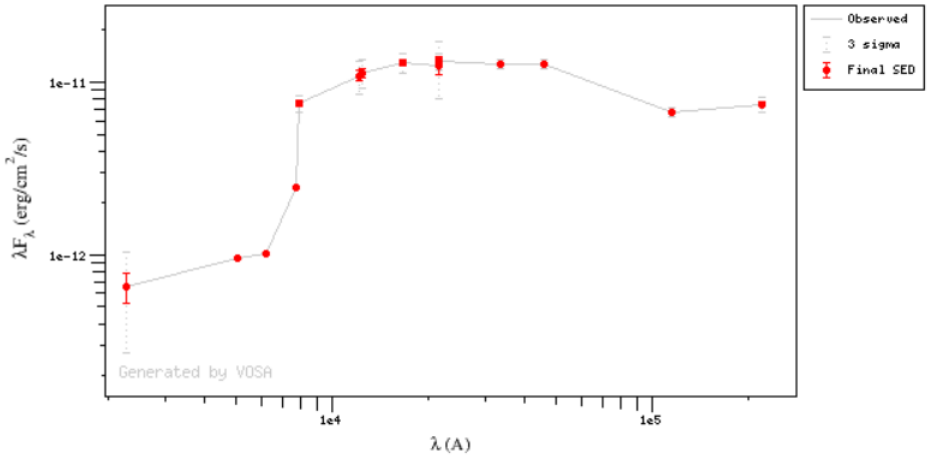

(b) Source coordinates: 285.79°, 4.44°

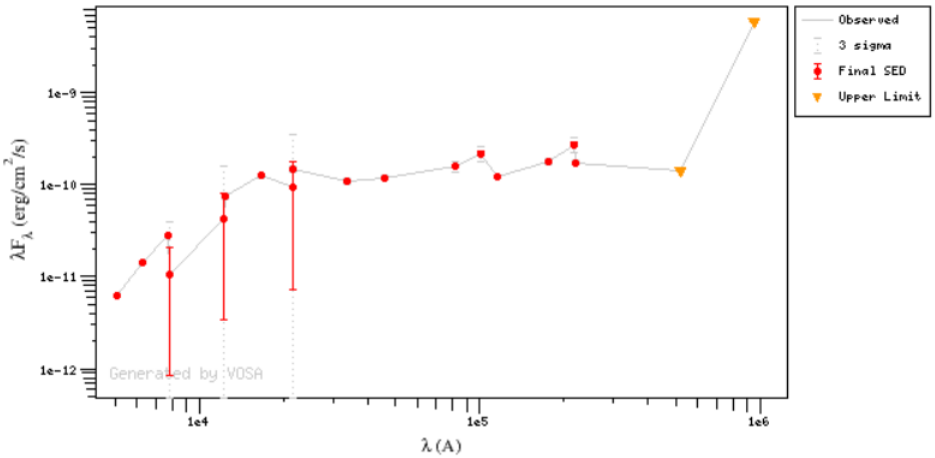

(c) Source coordinates: 285.87°, 4.62°

Figure 3.4: SEDs of the candidate YSOs associated with CS clumps in the Carina Flare supershell from the catalogue published by Marton et al. (2016) [2].

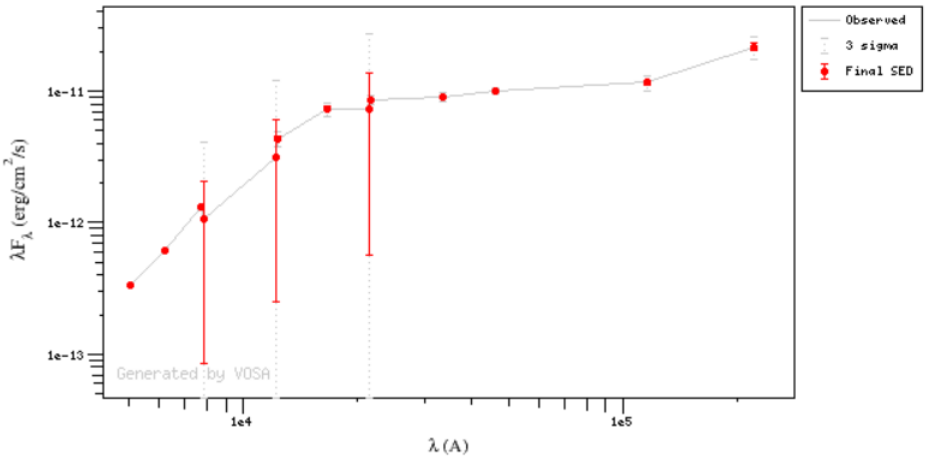

(a) Source coordinates: 285.90°, 4.50°

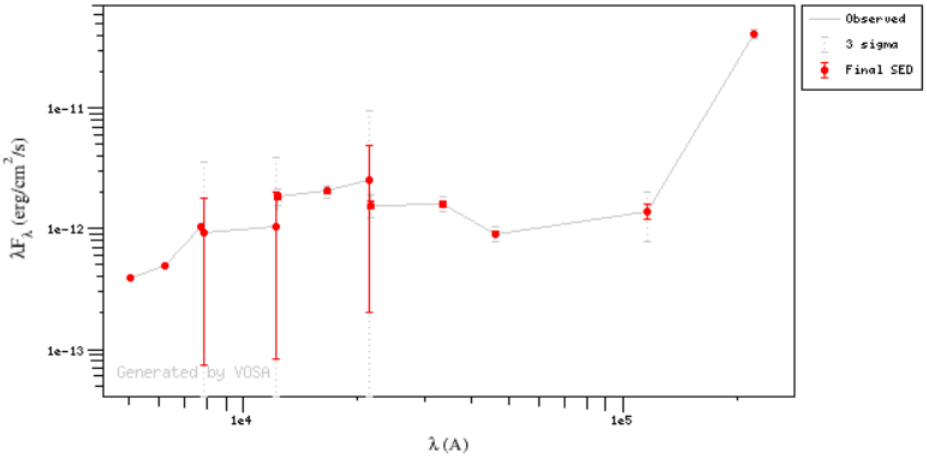

(b) Source coordinates: 285.89°, 4.501°

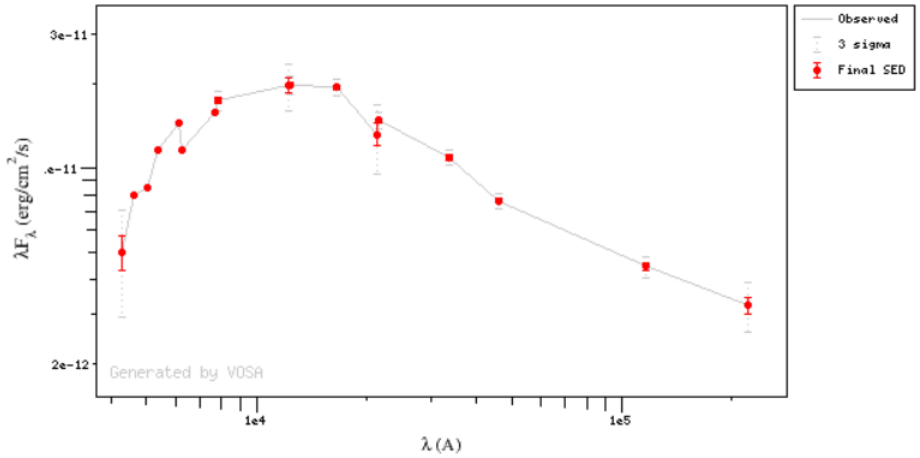

(c) Source coordinates: 285.91°, 4.47°

Figure 3.5: Marton's YSO candidate SEDs contd.

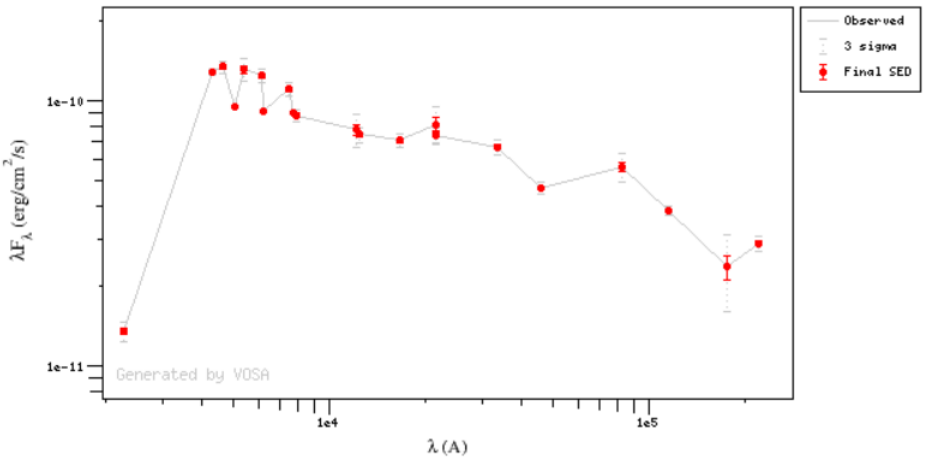

(a) Source coordinates: 285.94°, 4.45°

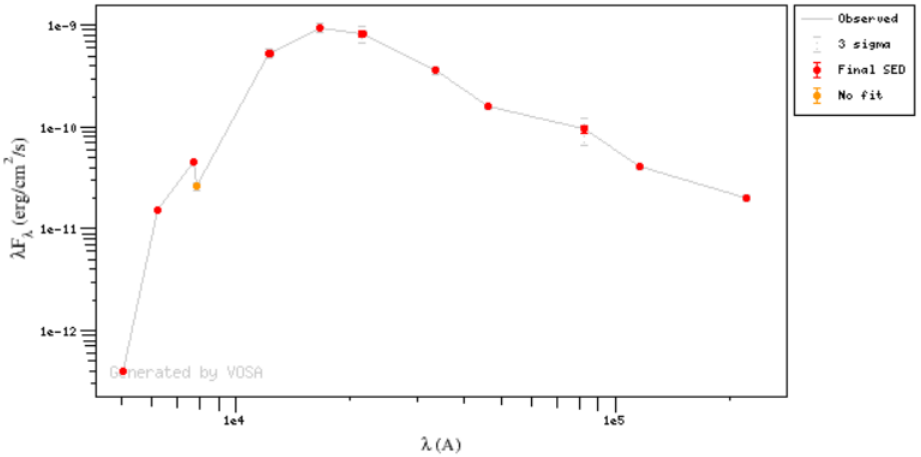

(b) Source coordinates: 285.95°, 4.52°

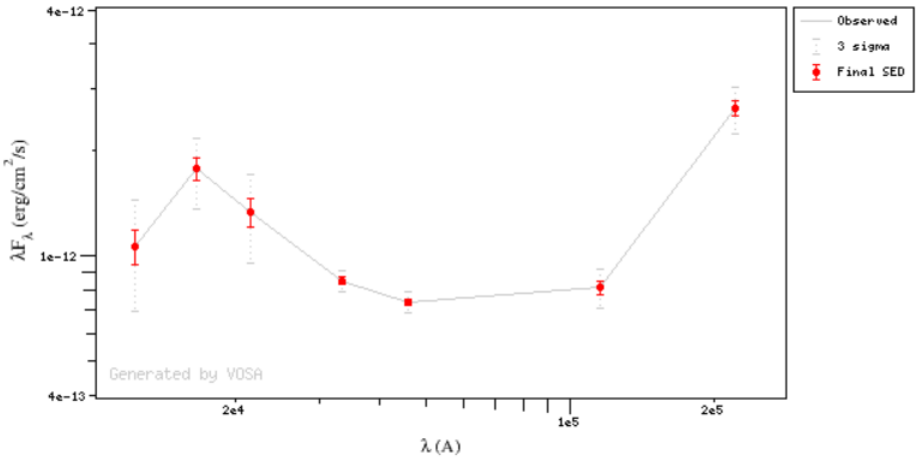

(c) Source coordinates: 288.32°, 7.26°

Figure 3.6: Marton's YSO candidate SEDs contd.

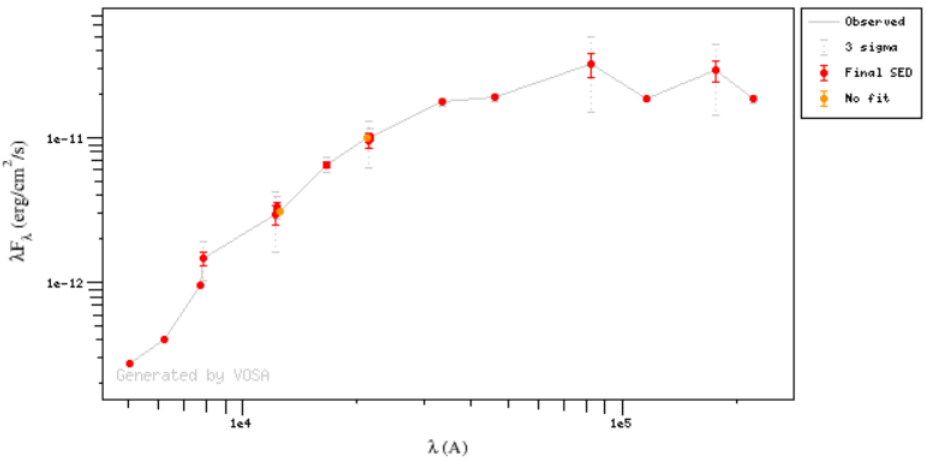

(a) Source coordinates: 288.32°, 7.26°

Figure 3.7: Marton's YSO candidate SEDs contd.

4

Analysis of CS Data

In this chapter, we present the results of CS observations conducted towards 5 molecular clouds associated with the "Carina Flare" supershell, and derive their physical parameters. As described in Section 2.1.3 the clouds were observed in the CS $J = 1 \rightarrow 0$ transition at 48.9 GHz, with observations targeted towards clouds previously detected in ^{12}CO, ^{13}CO and/or C^{18}O by Dawson et al. (2008a, 2008b, 2011a, 2011b) [8–10, 17]. The target regions are shown below in Figure 4.1.

4.1 CS Detections

The results of our observations are shown in Figure 4.2, which shows CS and CO contour maps overlaid on *WISE* band 4 images of our target regions. CS $J = 1 \rightarrow 0$ emission was significantly detected in 4 out of 5 regions. The figure shows the existence of dense gas at high altitude ($z \sim 330$ pc; 4.2(a)), as well as in the cloud that hosts the previously known star forming region and young cluster discussed in Dawson et al. (2011b; Fig. 4.2(b)). Note that in cases where there is more than one clump in the field, we name the clumps in alphabetical order from top to bottom in the integrated intensity image. In Fig 4.2(d), clump CS5b appears as central contiguous bright clump surrounded by small individual clumps. Since these clumps all occur at the same velocity and with the same line width, we consider it likely that they represent detected peaks of a single underlying structure, and therefore consider the group as one entity when computing physical properties below.

These detections are tabulated in Table 4.1: the first and second columns give the target field name and corresponding name of the parent cloud (from Dawson et al. (2008b) [9]); columns 3 – 5 lists previous detections in the ^{12}CO, ^{13}CO and CS $J = 1 \rightarrow 0$ lines, and column 6 lists CS detections. More detailed descriptions of the detected CS clumps are given further below.

4.2 Derived properties of the CS clumps

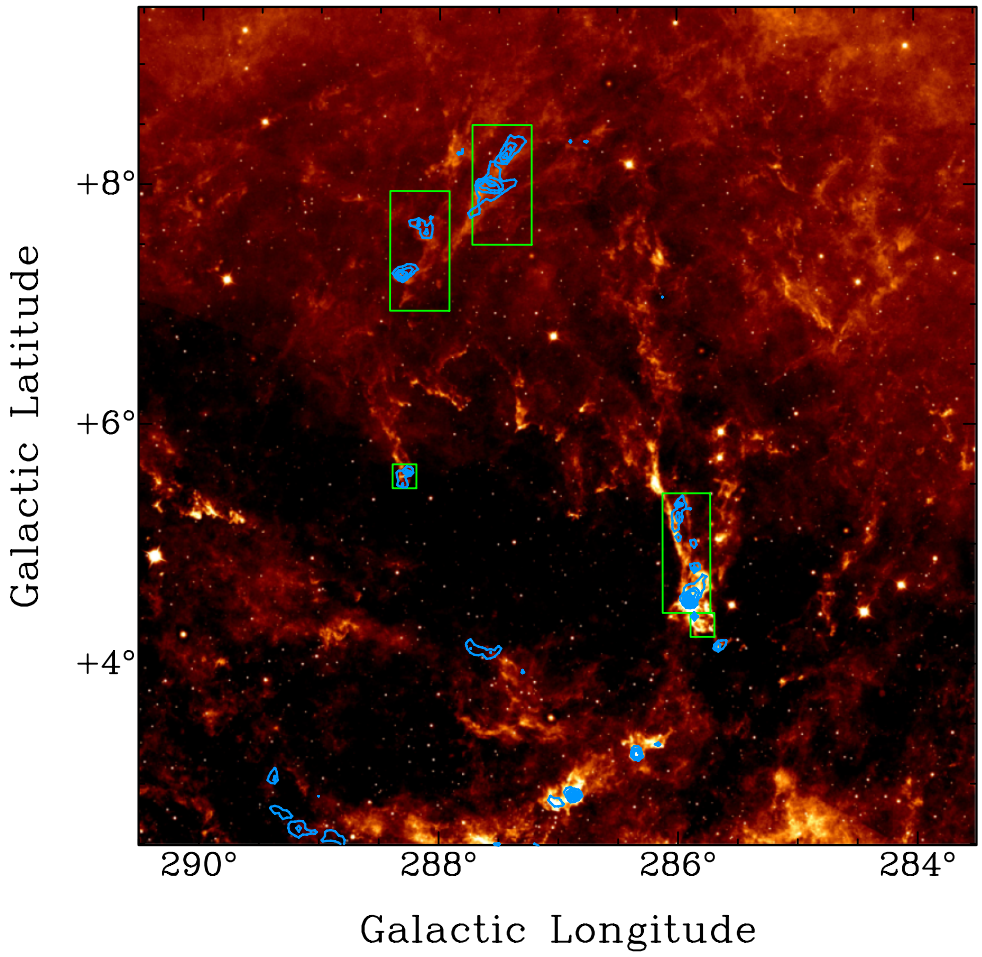

Figure 4.1: *WISE* band 4 (22 µm) image of the Carina Flare supershell overlaid with green boxes marking the fields for our CS observations done as an extension to the ongoing ATCA Legacy survey. The blue contours are NANTEN ^{13}CO $J = 1 \rightarrow 0$ integrated intensity from Dawson et al. (2008b), with contours drawn from 0.6 K km s^{-1} with increments of 1.0 K km s^{-1}.

4.2.1 CS molecular column density

We use the general equation 1.12 to calculate the column density of CS from its $J = 1 \rightarrow 0$ transition, assuming the rotational levels are in local thermodynamic equilibrium.

$$N_{Tot} = \frac{3h}{8\pi^3|\mu_{lu}|^2}\frac{Q_R}{g_u}e^{-E_l/k_BT_{exc}}\left(1-\exp\left(-\frac{h\nu_{ul}}{k_BT_{exc}}\right)\right)^{-1}\int \tau_v dv. \tag{4.1}$$

The properties of the CS $J = 1 \rightarrow 0$ transition involved in the above equation are listed below:

Table 4.1: Molecular detections in the selected test fields

Name	Parent ^{12}CO	Detection			
	cloud	^{12}CO	^{13}CO	C^{18}O	CS
CS1	288.30+7.27	Yes	Yes	Yes	Yes
CS2	285.90+4.53	Yes	Yes	Yes	Yes
CS3	288.27+5.60	Yes	Yes	Yes	Yes
CS4	285.90+4.53	Yes	Yes	No	No
CS5	287.60+8.00	Yes	Yes	Yes	Yes

- **Excitation Temperature**, T_{exc}: As mentioned in section 1.5.3, we use the *RADEX* statistical equilibrium radiative transfer code [37] to estimate a reasonable excitation temperature of the CS $J = 1 \rightarrow 0$ line, since it is likely to be sub-thermally excited. The input parameters are:

  1. Background Temperature, $T_{bg} = 2.73$ K is the CMB temperature.
  2. Kinetic Temperature, $T_k = 15$ K [7, 9].
  3. H_2 density = 10^4 cm^{-3} (critical density traced by $J = 1 \rightarrow 0$ from Table 1.1).
  4. Column density = 10^{13} cm^{-2}.
  5. Line Width = 0.9 km s^{-1} (the characteristic linewidth of our data).

  The above input parameters yield an excitation temperature of ~4 K for the CS $J = 1 \rightarrow 0$ transition line.

- **Degeneracies**: The total degeneracy of a rotational energy level is expressed as a product of the rotational degeneracies (g_J and g_K) and the spin degeneracy (g_I):

$$g_u \equiv g_J \, g_K \, g_I, \tag{4.2}$$

  where g_J is the rotational degeneracy that arises due to the projection of the angular momentum on the spatial axis z; g_K is the degeneracy associated with the internal quantum number K in symmetric and asymmetric top molecules due to projection of the angular momentum on the molecular axis; and g_I is the nuclear spin degeneracy [36]. For CS, which is a linear molecule:

  1. $g_J = 2J_u + 1$ (J_u is the rotational quantum number of the upper energy level). The value of $J_u = 1$ for the $1 \rightarrow 0$ transition. Hence $g_J = 3$.
  2. $g_K = 1$ (for linear molecules).

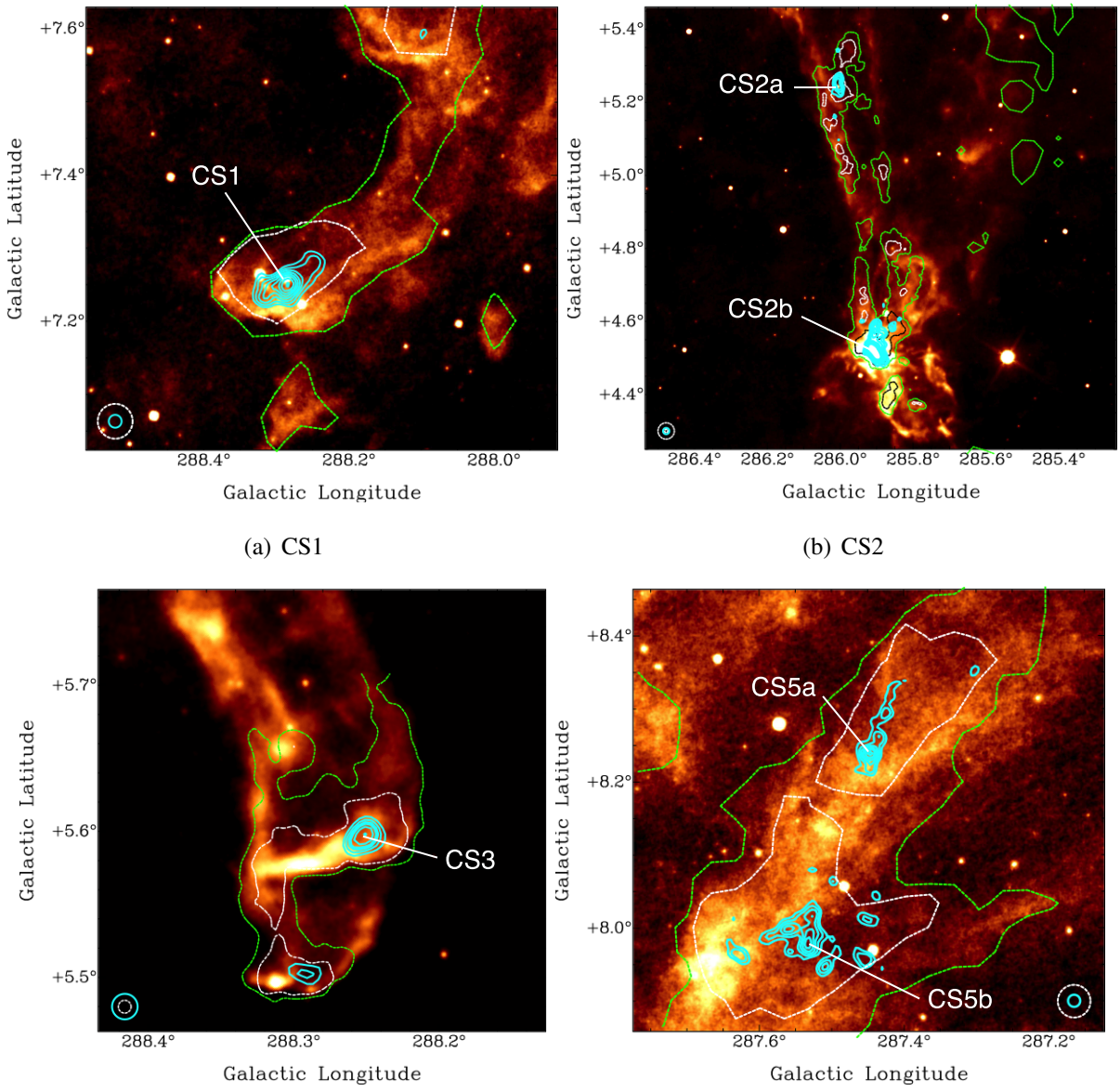

(a) CS1 (b) CS2

(c) CS3 (d) CS5

Figure 4.2: New CS $J = 1 \rightarrow 0$ integrated intensity contours (solid light blue) and archival ^{12}CO $J = 1 \rightarrow 0$ (dashed green) and ^{13}CO $J = 1 \rightarrow 0$ integrated intensity contours (dashed white or black) overlaid on *WISE* band 4 images of the clouds associated with the Carina Flare supershell. The lowest CS contour level is at 0.25, 0.35, 0.36, and 0.23 K km s^{-1} for panels (a), (b), (c) and (d) respectively and incremented in steps of 0.05 K km s^{-1}. ^{12}CO and ^{13}CO contours are plotted only at the 3σ detection limits for each dataset – 1.2 and 0.7 K km s^{-1} for NANTEN and 3.0 and 1.2 K km s^{-1} for Mopra. Panels (a) and (d) use only NANTEN data, panel (c) uses only Mopra data, and panel (b) uses Mopra data for the left-hand filamentary cloud and NANTEN data for the upper right portion of the image. HPBWs are plotted in the lower corners of the images.

3. $g_I = 1$ (for linear molecules).

- **Rotational Partition Function**: We derived the rotational partition function for CS (a linear molecule), assuming rigid rotor approximation to the energy levels.

$$Q_R = \frac{k_B T_{exc}}{h B_0}, \tag{4.3}$$

where $k_B = 1.38 \times 10^{-23}\,\mathrm{J\,K^{-1}}$ is the Boltzmann constant; $T_{exc} = 4\,\mathrm{K}$ is the excitation temperature of the transition, $h = 6.626 \times 10^{-34}\,\mathrm{J\,s}$ is Planck's constant and $B_0 = 24495.592 \pm 0.006$ MHz is the ground state rotational constant (Kewly et al. (1963) - Millimeter Wave Spectroscopy of Unstable Molecular Species. I. Carbon Monosulfide).

- **Dipole moment matrix element**: For linear molecules, the dipole moment matrix element is given by:

$$|\mu_{lu}|^2 = \mu^2 S, \tag{4.4}$$

where S is the line strength and μ is the permanent dipole moment of the molecule. For the CS $J = 1 \longrightarrow 0$ transition,

$$S = \frac{J_u}{2J_u + 1}$$
$$\mu = 1.98 \text{ Debye}.$$

Using these above properties we derived CS column density images from our 3-dimensional datacubes. For each cube, we inspected the data to determine a velocity range over which emission was detected, and produced integrated-intensity maps for that range. Column density values were computed only for "detected" pixels, defined as those showing emission above the 3σ level in integrated intensity. τ_v was computed from the observed T_R^* for each voxel in the relevant velocity range using equation 1.22, and summed to compute the integral in equation 4.1. This produced a CS column density for each position, which was converted to a molecular column density, $N(\mathrm{H_2})$, assuming an abundance ratio of CS to $\mathrm{H_2}$ of $[\mathrm{CS}]/[\mathrm{H_2}] \sim 10^{-9}$ [31].

4.2.2 LTE Mass

We calculate the LTE mass, the CS luminosity mass of the clump, by summing $\mathrm{H_2}$ column densities across all pixels in each molecular clump:

$$M_{LTE} = \mu\, m_{\rm H} \sum [D(\Delta\Omega_i)]^2\, N({\rm H}_{2,i}), \tag{4.5}$$

where the M_{LTE} is the CS luminosity based mass of the clump; the molecular weight, $\mu = 2.7$ accounts for the presence of helium and heavier elements; $D = 2.6$ kpc is the distance to the molecular clump; $\Delta\Omega_i$ is the angular size of the pixel i in radians; and $N(\mathrm{H}_{2,i})$ is the column density of pixel i. Here we define "clumps" as contiguous regions of emission above the 4σ detection limit in integrated intensity, where σ is the standard deviation in integrated intensity map over a typical line width in emission-free section of the datacube. The exception to this is CS5b, where (as discussed above) we do not require the emission to be contiguous, and treat all detected emission in the vicinity of the largest clump as one entity. The derived LTE masses for each CS clump are given in Table 4.2, in units of solar mass, $M_\odot$.

Table 4.2: Physical parameters derived from CS observations

	Clump	LTE mass ($M_\odot$) ($T_{ex} = 4$ K)	Virial mass ($M_\odot$)	Clump area (pc^2)	Position (l, b) (degree)
CS1	a	899	273	7	(288.28°, 7.25°)
CS2	a	73	78	0.7	(286.01°, 5.25°)
	b	1634	926	10	(285.9°, 4.53°)
CS3	a	83	65	0.8	(285.25°, 5.59°)
CS5	a	216	188	1.7	(287.43°, 8.27°)
	b	460	649	7	(287.53°, 7.99°)

4.2.3 Virial Mass

The mass required for a cloud to be self-gravitating against its own internal velocity dispersion is known as the Virial mass. To calculate the Virial mass of our CS clumps we adopt the formula from Dawson et al. (2008b). It is a simple formulation that assumes a spherical cloud with a $1/r$ density distribution, and ignores the effect of external pressure and magnetic fields, only incorporating the gravitational and internal pressure [9]:

$$\frac{M_{vir}}{M_\odot} = 190\, R\, (\Delta v)^2, \tag{4.6}$$

where R is the effective radius in parsecs and Δv is the cloud velocity dispersion in $\mathrm{km\,s^{-1}}$ [9]. The radius R of the clump is computed from $\sqrt{A/\pi}$, where A is the area of all detected pixels, and Δv

is the FWHM of a Gaussian fit to the mean of all detected spectra. The derived Virial masses for each CS clump are given in Table 4.2 (in units of solar mass, $M_{\odot}$), together with the projected area of the clump in parsecs.

5

Discussion and Interpretation

Figure 5.1 shows the detected CS clumps from Chapter 4 overlaid with the YSO candidates described in Chapter 3.

5.1 Gravitational Stability of the CS Clumps and Connection to Star Formation Activity

The comparison between the luminosity-based LTE mass and the Virial mass of the clump is often used as a tool to gauge gravitational stability. One way to do this is to define the Virial parameter, which measures the ratio of the kinetic and the gravitational energy of the clump [62]. It is defined as, $\alpha \equiv 5{\sigma_v}^2 R/GM$ [63], where M, R and ${\sigma_v}^2$ are the fragment's mass, radius and the the one-dimensional velocity dispersion respectively. For given environmental conditions it is possible to define a critical value of the Virial parameter (α_{crit}) such that a clump with $\alpha > \alpha_{crit}$ is charaterised as a "subcritical cloud" (gravitationally unbound and may diffuse back into the ISM), while a clump with $\alpha < \alpha_{crit}$ "supercritical" (gravitationally bound or marginally bound and has the potential to collapse to stellar cores). For a non-magnetised cloud/clump $\alpha_{crit} \gtrsim 2$ (for comprehensive details of the mathematical formulation refer to Kauffmann et al. 2013 [62]).

However, here we use a very simplistic approach to assess the "virialisation" of the CS clumps. This analysis technique is the same as employed by Dawson et al. (2008b) [9] to the molecular clouds detected in the ^{12}CO and ^{13}CO $J = 1 \rightarrow 0$ lines. Since we are investigating the clouds from the same catalogue [9] but at sub-parsec scale and in a denser gas tracer, we decided to use the Dawson et al. (2008b) version of the "Virial analysis". In this analysis, if the LTE mass of the clump is greater than or equal to its Virial mass, the clump is assumed to be "Virialised". Under this formulation, none of the ^{12}CO and ^{13}CO clouds previously catalogued [9, 17] in the Carina Flare supershell are found

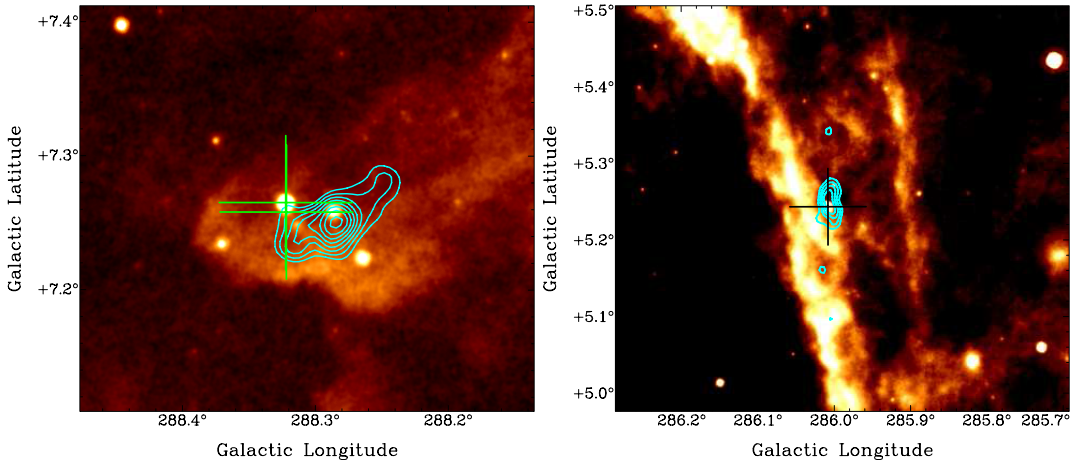

(a) CS1

(b) CS2a

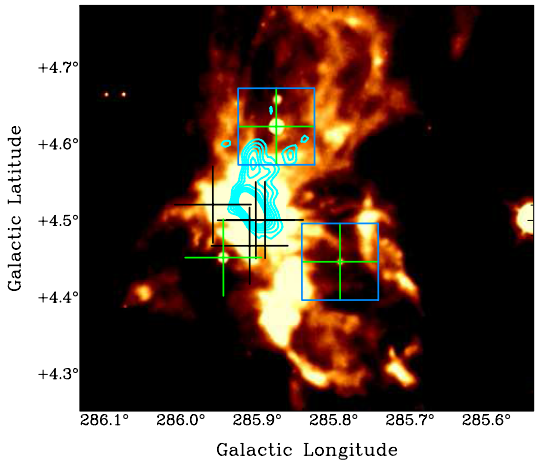

(c) CS2b

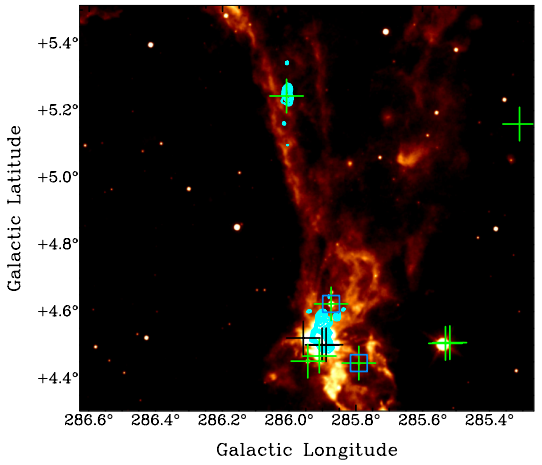

(d) CS2a and CS2b

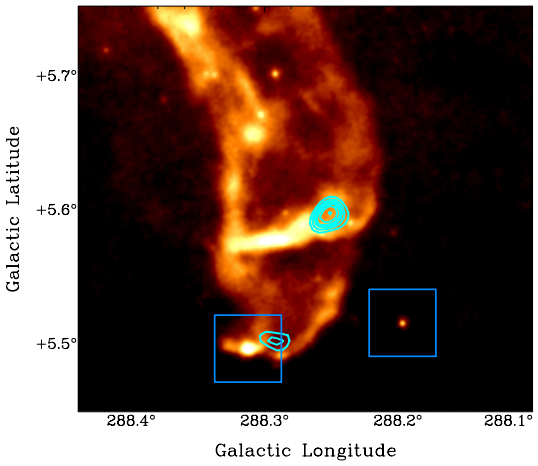

(e) CS3

Figure 5.1: CS $J = 1 \rightarrow 0$ integrated intensity contours (solid light blue), Marton et al. (2016) YSOs (green or black crosses) and YSOs identified using the K14 classification scheme (blue boxes) overlaid on *WISE* band 4 images. The CS contour levels are the as Fig.4.2

to be globally self-gravitating. Note that while adopting this analysis technique, we are aware of its shortcomings, and recognise that fulfilling this condition does not always imply a truly bound object.

On inspecting the values in Table 4.2, it is evident that all but two of the clumps in our small sample are virialised under the simple formulation described above. Furthermore, while Clump CS2a (Fig. 4.2(b)) is technically sub-virialised, the difference between the LTE and Virial masses for this clump (M_{LTE} = 73 vs M_{vir} = 78 $M_{\odot}$) are so small as to be negligible. In fact, its position is coincident with one of the YSOs from Marton's YSO catalogue (Fig. 5.1(b)), strongly suggesting that star-formation is in fact occurring. We interpret this as a new detection of likely star-formation activity in the supershell, and at a moderately high altitude of $z \sim 230$pc.

Moving to the second clump in the same field, clump CS2b; prior studies (e.g. Dawson et al. (2011b) [17]) reveal that it is host to a young emerging cluster (Fig 5.1(c)). Six YSO candidates are detected in and around this clump, and its LTE mass is $\sim$ 50% larger than its Virial mass – consistent with the on-going star formation activity.

Clump CS1a shows two young stellar object candidates close to a dense gas clump that is the most highly virialised (Fig 5.1(a)) object in our sample. This clump resides inside one of the two high-altitude clouds investigated using the ATCA Legacy survey, and at $z \sim 330$ pc is now the highest altitude star-forming region discovered in the Carina Flare supershell.

Similarly, the LTE and virial masses of the CS5a clump indicate that it is virialised, unlike its counterpart in the field, CS5b. In the integrated map this clump (CS5b) appears as a large and somewhat extended clump surrounded by $\sim$ 4 smaller clumps. As discussed above, when computing the properties of this emission we consider it as one entity representing an underlying contiguous structure whose peaks are detected in the mountainous landscape of the parent molecular cloud. This may have lead to over-estimations of the virial mass with respect to the LTE mass. In either case, no young stellar objects are identified in either CS5a and b, consistent with a picture in which this high-altitude ($z \sim 370$pc) material is not currently actively forming stars.

Finally, the CS3 clump is virialised under our formulation, and two YSO candidates are detected in the field, although neither are coincident with the clump. One of the YSO candidates lies outside the main emission of the shell wall and is not am embedded YSO. From Fig. 5.1(e), we can also see a small quantity of dense gas (not identified as a clump) to the right of the YSO that appears as a weak detection in the integrated intensity maps.

5.2 Comments on the Two YSO Identification Schemes

Overall, there are $\sim$ 47 YSO candidates from Marton et al's (2016) catalogue in the region $b \gtrsim 3$, compared to 22 sources identified by the K14 classification scheme. Marton's machine learning approach was more successful at identifying YSO candidates coincident (or close to) our newly detected dense gas clumps (10 sources vs 4 sources; two in common.) The four YSO candidates identified by the K14 classification scheme are coincident with the clouds, G285.90+4.53 and G288.27+5.60, the former of which is already identified as actively star-forming, and the latter of which hosts an IRAS YSO candidate [10, 17]. On the other hand, the K14 classification scheme only identified two YSO candidates near the CS2b clump in G285.90+4.53, and rejected the highly luminous region hosting the cluster itself as an extended object. However, this algorithm also identified a point source (coordinates: 288.31°, 5.49°) in the vicinity of the CS3 clump and classified it as a Class I YSO candidate. Conversely, the Marton machine learning approach was better able to classify sources within the complex and confused active star-forming region of the CS2b clump, and identified several completely new YSO candidates coincident with CS clumps in regions previously unknown to be star-forming. This appears to show the advantages of machine learning techniques compared to conventional color-color cuts.

6

Conclusions and Future Work

In this work we have discovered that dense gas (as traced by CS $J = 1 \rightarrow 0$) exists in the molecular clouds associated with the high-altitude portions of the Galactic Supershell GSH 287+04−17, also known as the Carina Flare Supershell. We have also newly identified a population of YSO candidates in the region using the *ALLWISE* catalogue, and have investigated their distribution with respect to the CS clumps.

The close association between the dense gas traced by CS and the young stellar objects provides substantial evidence in support of on-going star formation activity in the Carina Flare molecular clouds. As has been discussed in previous studies, this star formation may have been triggered by the supershell – either in the sense that star-forming molecular gas was born within it, or in the sense that previously existing molecular gas may have been compressed to induce star formation.

Two key findings are new to this work. Firstly, several-thousand solar masses of dense gas have been discovered associated with the high-altitude portions of a known Galactic supershell ($z \sim 200$–400 pc); secondly, there is evidence for ongoing star formation activity in much of this gas. This is evidenced both by the association of YSO candidates, and by the suggestion that many of the CS clumps are likely to be gravitationally bound. Furthermore, we have discovered likely star formation at far higher altitudes than previously known in this region, with two YSOs and a virialised CS clump seen at $z \sim 330$ pc above the Midplane.

The next stage of this work will be to obtain bolometric luminosity estimates for the YSOs, to determine their masses. A possible way to approach this would be to improve the SEDs presented in this work with the addition of longer wavelength data. This could be in theory extracted from properly-calibrated FIR images if point-source data is not available. From past work, it is known that massive (at least early B-type) star formation is occurring in clump CS2b [17], which is also a bright region in *WISE* 22 µm images. From the lack of similarly bright emission in the rest of the studied

region, it may be unlikely that such activity is occurring elsewhere in high altitude clouds. However, bolometric luminosities would still be useful to better characterise the population of YSOs.

In the longer-term future, this work may be extended to study the high altitude regions of the Milky Way Galaxy as a whole, so as to draw statistically significant conclusions about the rate of star formation activity near the Disk-Halo interface of the Milky Way. This study may help gain useful insight not only into the origin of halo stars but also about the disk - halo interaction which forms an integral part of galaxy evolution.

References

[1] X. P. Koenig and D. T. Leisawitz. *A Classification Scheme for Young Stellar Objects Using the Wide-field Infrared Survey Explorer AllWISE Catalog: Revealing Low-density Star Formation in the Outer Galaxy*. ApJ**791**, 131 (2014). 1407.2262.

[2] G. Marton, L. V. Tóth, R. Paladini, M. Kun, S. Zahorecz, P. McGehee, and C. Kiss. *An all-sky support vector machine selection of WISE YSO candidates*. MNRAS**458**, 3479 (2016). 1602.05777.

[3] L. Chen, J. L. Hou, and J. J. Wang. *On the Galactic Disk Metallicity Distribution from Open Clusters. I. New Catalogs and Abundance Gradient*. AJ**125**, 1397 (2003). astro-ph/0212542.

[4] S. Malhotra. *The vertical equilibrium of molecular gas in the Galactic disk*. ApJ**433**, 687 (1994). astro-ph/9404028.

[5] J. Kerp, D. Lenz, and T. Röhser. *Star formation in a diffuse high-altitude cloud?* A&A**589**, A123 (2016). 1603.05396.

[6] R. de la Fuente Marcos and C. de la Fuente Marcos. *Present-Day Star Formation at High Galactic Altitude: The Tidal Encounter Paradigm*. ApJ**685**, L125 (2008).

[7] Y. Fukui, T. Onishi, R. Abe, A. Kawamura, K. Tachihara, R. Yamaguchi, A. Mizuno, and H. Ogawa. *Discovery of the Carina Flare with NANTEN; Evidence for a Supershell That Triggered the Formation of Stars and Massive Molecular Clouds*. PASJ**51**, 751 (1999).

[8] J. R. Dawson, N. Mizuno, T. Onishi, N. M. McClure-Griffiths, and Y. Fukui. *The 'Carina Flare' supershell: probing the atomic and molecular ISM in a Galactic chimney*. MNRAS**387**, 31 (2008). 0802.4463.

[9] J. R. Dawson, A. Kawamura, N. Mizuno, T. Onishi, and Y. Fukui. *Catalogue of $^{12}CO(J = 1\text{-}0)$ and $^{13}CO(J = 1\text{-}0)$ Molecular Clouds in the Carina Flare Supershell*. PASJ**60**, 1297 (2008). 0808.3850.

[10] J. R. Dawson, N. M. McClure-Griffiths, A. Kawamura, N. Mizuno, T. Onishi, A. Mizuno, and Y. Fukui. *Supershells as Molecular Cloud Factories: Parsec Resolution Observations of H I and ^{12}CO(J = 1-0) in GSH 287+04-17 and GSH 277+00+36*. ApJ**728**, 127 (2011). 1012.5363.

[11] E. L. Wright, P. R. M. Eisenhardt, A. K. Mainzer, M. E. Ressler, R. M. Cutri, T. Jarrett, J. D. Kirkpatrick, D. Padgett, R. S. McMillan, M. Skrutskie, S. A. Stanford, M. Cohen, R. G. Walker, J. C. Mather, D. Leisawitz, T. N. Gautier, III, I. McLean, D. Benford, C. J. Lonsdale, A. Blain, B. Mendez, W. R. Irace, V. Duval, F. Liu, D. Royer, I. Heinrichsen, J. Howard, M. Shannon, M. Kendall, A. L. Walsh, M. Larsen, J. G. Cardon, S. Schick, M. Schwalm, M. Abid, B. Fabinsky, L. Naes, and C.-W. Tsai. *The Wide-field Infrared Survey Explorer (WISE): Mission Description and Initial On-orbit Performance*. AJ**140**, 1868 (2010). 1008.0031.

[12] T. P. Robitaille, B. A. Whitney, R. Indebetouw, and K. Wood. *Interpreting Spectral Energy Distributions from Young Stellar Objects. II. Fitting Observed SEDs Using a Large Grid of Precomputed Models*. ApJS**169**, 328 (2007). astro-ph/0612690.

[13] M. Burton, R. Crocker, J. Dickey, M. Filipovic, C. Purcell, J. Rathborne, G. Rowell, N. Tothill, and A. Walsh. *The Interstellar Medium White Paper*. ArXiv e-prints (2013). 1307.0712.

[14] Y.-H. Chu. *Bubbles and Superbubbles: Observations and Theory*. In F. Bresolin, P. A. Crowther, and J. Puls, eds., *Massive Stars as Cosmic Engines*, vol. 250 of *IAU Symposium*, pp. 341–354 (2008).

[15] C. Heiles. *H I shells, supershells, shell-like objects, and 'worms'*. ApJS**55**, 585 (1984).

[16] J. R. Dawson. *The Supershell - Molecular Cloud Connection: Large-Scale Stellar Feedback and the Formation of the Molecular ISM*. PASA**30**, e025 (2013). 1301.1419.

[17] J. R. Dawson, N. M. McClure-Griffiths, J. M. Dickey, and Y. Fukui. *Molecular Clouds in Supershells: A Case Study of Three Objects in the Walls of GSH 287+04-17 and GSH 277+00+36*. ApJ**741**, 85 (2011). 1108.3882.

[18] C. M. Dutra, E. Bica, J. Soares, and B. Barbuy. *New infrared star clusters in the southern Milky Way with 2MASS*. A&A**400**, 533 (2003). astro-ph/0301221.

[19] J. B. Soares, E. Bica, A. V. Ahumada, and J. J. Clariá. *Near infrared photometric and optical spectroscopic study of 22 low mass star clusters embedded in nebulae*. A&A**478**, 419 (2008).

[20] X. P. Koenig, D. T. Leisawitz, D. J. Benford, L. M. Rebull, D. L. Padgett, and R. J. Assef. *Wide-field Infrared Survey Explorer Observations of the Evolution of Massive Star-forming Regions*. ApJ**744**, 130 (2012).

[21] H. C. van de Hulst. *1945, The Origin of Radio Waves from Space*, p. 302 (1982).

[22] G. J. Madsen and R. J. Reynolds. *An Investigation of Diffuse Interstellar Gas toward a Large, Low-Extinction Window into the Inner Galaxy*. ApJ**630**, 925 (2005). astro-ph/0505485.

[23] L. M. Haffner, R.-J. Dettmar, J. E. Beckman, K. Wood, J. D. Slavin, C. Giammanco, G. J. Madsen, A. Zurita, and R. J. Reynolds. *The warm ionized medium in spiral galaxies*. Reviews of Modern Physics **81**, 969 (2009). 0901.0941.

[24] J. M. Shull and S. Beckwith. *Interstellar molecular hydrogen*. ARA&A**20**, 163 (1982).

[25] S. C. O. Glover and M.-M. Mac Low. *On the relationship between molecular hydrogen and carbon monoxide abundances in molecular clouds*. MNRAS**412**, 337 (2011). 1003.1340.

[26] S. Weinreb, A. H. Barrett, M. L. Meeks, and J. C. Henry. *Radio Observations of OH in the Interstellar Medium*. Nat**200**, 829 (1963).

[27] A. C. Cheung, D. M. Rank, C. H. Townes, D. D. Thornton, and W. J. Welch. *Detection of NH_3 Molecules in the Interstellar Medium by Their Microwave Emission*. Physical Review Letters **21**, 1701 (1968).

[28] A. C. Cheung, D. M. Rank, C. H. Townes, D. D. Thornton, and W. J. Welch. *Detection of Water in Interstellar Regions by its Microwave Radiation*. Nat**221**, 626 (1969).

[29] L. E. Snyder, D. Buhl, B. Zuckerman, and P. Palmer. *Microwave Detection of Interstellar Formaldehyde*. Physical Review Letters **22**, 679 (1969).

[30] R. W. Wilson, K. B. Jefferts, and A. A. Penzias. *Carbon Monoxide in the Orion Nebula*. ApJ**161**, L43 (1970).

[31] N. Maxted, M. Burton, C. Braiding, G. Rowell, H. Sano, F. Voisin, M. Capasso, G. Pühlhofer, and Y. Fukui. *Probing the local environment of the supernova remnant HESS J1731-347 with CO and CS observations*. MNRAS**474**, 662 (2018). 1710.06101.

[32] K. Dobashi, J.-P. Bernard, and Y. Fukui. *Molecular Clouds in Cygnus. II. Statistical Studies of Star-forming Regions*. ApJ**466**, 282 (1996).

[33] G. Kelly, S. Viti, E. Bayet, R. Aladro, and J. Yates. *Mapping CS in starburst galaxies: Disentangling and characterising dense gas*. A&A**578**, A70 (2015). 1502.04601.

[34] S. Zhou, N. J. Evans, II, R. Guesten, L. G. Mundy, and M. L. Kutner. *CS multitransitional studies of density distribution in star-forming regions. I - The NGC 2071 region*. ApJ**372**, 518 (1991).

[35] H. A. Thronson, Jr. and C. J. Lada. *A search for high-velocity carbon monosulfide emission in star-forming regions*. ApJ**284**, 135 (1984).

[36] J. G. Mangum and Y. L. Shirley. *How to Calculate Molecular Column Density*. PASP**127**, 266 (2015). 1501.01703.

[37] F. F. S. van der Tak, J. H. Black, F. L. Schöier, D. J. Jansen, and E. F. van Dishoeck. *A computer program for fast non-LTE analysis of interstellar line spectra. With diagnostic plots to interpret observed line intensity ratios*. A&A**468**, 627 (2007). 0704.0155.

[38] S. Molinari, S. Pezzuto, R. Cesaroni, J. Brand, F. Faustini, and L. Testi. *The evolution of the spectral energy distribution in massive young stellar objects*. A&A**481**, 345 (2008).

[39] C. J. Lada. *Star formation - From OB associations to protostars*. In M. Peimbert and J. Jugaku, eds., *Star Forming Regions*, vol. 115 of *IAU Symposium*, pp. 1–17 (1987).

[40] B. A. Whitney, K. Wood, J. E. Bjorkman, and M. Cohen. *Two-dimensional Radiative Transfer in Protostellar Envelopes. II. An Evolutionary Sequence*. ApJ**598**, 1079 (2003). astro-ph/0309007.

[41] B. A. Whitney, K. Wood, J. E. Bjorkman, and M. J. Wolff. *Two-dimensional Radiative Transfer in Protostellar Envelopes. I. Effects of Geometry on Class I Sources*. ApJ**591**, 1049 (2003). astro-ph/0303479.

[42] B. A. Whitney, R. Indebetouw, J. E. Bjorkman, and K. Wood. *Two-Dimensional Radiative Transfer in Protostellar Envelopes. III. Effects of Stellar Temperature*. ApJ**617**, 1177 (2004).

[43] T. P. Robitaille, B. A. Whitney, R. Indebetouw, K. Wood, and P. Denzmore. *Interpreting Spectral Energy Distributions from Young Stellar Objects. I. A Grid of 200,000 YSO Model SEDs*. ApJS**167**, 256 (2006). astro-ph/0608234.

[44] B. A. Wilking. *The formation of low-mass stars*. PASP**101**, 229 (1989).

[45] P. Andre, D. Ward-Thompson, and M. Barsony. *Submillimeter continuum observations of Rho Ophiuchi A - The candidate protostar VLA 1623 and prestellar clumps*. ApJ**406**, 122 (1993).

[46] C. J. Lada and N. D. Kylafis, eds. *The Origin of Stars and Planetary Systems*, vol. 540 of *NATO Advanced Science Institutes (ASI) Series C* (1999).

[47] C. J. Lada and F. C. Adams. *Interpreting infrared color-color diagrams - Circumstellar disks around low- and intermediate-mass young stellar objects*. ApJ**393**, 278 (1992).

[48] L. E. Allen, N. Calvet, P. D'Alessio, B. Merin, L. Hartmann, S. T. Megeath, R. A. Gutermuth, J. Muzerolle, J. L. Pipher, P. C. Myers, and G. G. Fazio. *Infrared Array Camera (IRAC) Colors of Young Stellar Objects*. ApJS**154**, 363 (2004).

[49] N. M. McClure-Griffiths, J. M. Dickey, B. M. Gaensler, A. J. Green, M. Haverkorn, and S. Strasser. *The Southern Galactic Plane Survey: H I Observations and Analysis*. ApJS**158**, 178 (2005). astro-ph/0503134.

[50] N. M. McClure-Griffiths, D. J. Pisano, M. R. Calabretta, H. A. Ford, F. J. Lockman, L. Staveley-Smith, P. M. W. Kalberla, J. Bailin, L. Dedes, S. Janowiecki, B. K. Gibson, T. Murphy, H. Nakanishi, and K. Newton-McGee. *Gass: The Parkes Galactic All-Sky Survey. I. Survey Description, Goals, and Initial Data Release*. ApJS**181**, 398 (2009). 0901.1159.

[51] P. M. W. Kalberla, N. M. McClure-Griffiths, D. J. Pisano, M. R. Calabretta, H. A. Ford, F. J. Lockman, L. Staveley-Smith, J. Kerp, B. Winkel, T. Murphy, and K. Newton-McGee. *GASS: the Parkes Galactic all-sky survey. II. Stray-radiation correction and second data release*. A&A**521**, A17 (2010). 1007.0686.

[52] R. Wünsch, P. Jáchym, V. Sidorin, S. Ehlerová, J. Palouš, J. Dale, J. R. Dawson, and Y. Fukui. *The Carina Flare. What can fragments in the wall tell us?* A&A**539**, A116 (2012). 1111.4391.

[53] R. M. Cutri, E. L. Wright, T. Conrow, J. W. Fowler, P. R. M. Eisenhardt, C. Grillmair, J. D. Kirkpatrick, F. Masci, H. L. McCallon, S. L. Wheelock, S. Fajardo-Acosta, L. Yan, D. Benford, M. Harbut, T. Jarrett, S. Lake, D. Leisawitz, M. E. Ressler, S. A. Stanford, C. W. Tsai, F. Liu, G. Helou, A. Mainzer, D. Gettings, A. Gonzalez, D. Hoffman, K. A. Marsh, D. Padgett, M. F. Skrutskie, R. P. Beck, M. Papin, and M. Wittman. *Explanatory Supplement to the AllWISE Data Release Products*. Tech. rep. (2013).

[54] A. Mainzer, J. Bauer, T. Grav, J. Masiero, R. M. Cutri, J. Dailey, P. Eisenhardt, R. S. McMillan, E. Wright, R. Walker, R. Jedicke, T. Spahr, D. Tholen, R. Alles, R. Beck, H. Brandenburg, T. Conrow, T. Evans, J. Fowler, T. Jarrett, K. Marsh, F. Masci, H. McCallon, S. Wheelock, M. Wittman, P. Wyatt, E. DeBaun, G. Elliott, D. Elsbury, T. Gautier, IV, S. Gomillion, D. Leisawitz, C. Maleszewski, M. Micheli, and A. Wilkins. *Preliminary Results from NEOWISE: An Enhancement to the Wide-field Infrared Survey Explorer for Solar System Science*. ApJ**731**, 53 (2011). 1102.1996.

[55] R. M. Cutri and et al. *VizieR Online Data Catalog: WISE All-Sky Data Release (Cutri+ 2012)*. VizieR Online Data Catalog **2311** (2012).

[56] M. F. Skrutskie, R. M. Cutri, R. Stiening, M. D. Weinberg, S. Schneider, J. M. Carpenter, C. Beichman, R. Capps, T. Chester, J. Elias, J. Huchra, J. Liebert, C. Lonsdale, D. G. Monet, S. Price, P. Seitzer, T. Jarrett, J. D. Kirkpatrick, J. E. Gizis, E. Howard, T. Evans, J. Fowler, L. Fullmer, R. Hurt, R. Light, E. L. Kopan, K. A. Marsh, H. L. McCallon, R. Tam, S. Van Dyk, and S. Wheelock. *The Two Micron All Sky Survey (2MASS)*. AJ**131**, 1163 (2006).

[57] R. M. Cutri, M. F. Skrutskie, S. van Dyk, C. A. Beichman, J. M. Carpenter, T. Chester, L. Cambresy, T. Evans, J. Fowler, J. Gizis, E. Howard, J. Huchra, T. Jarrett, E. L. Kopan, J. D. Kirkpatrick, R. M. Light, K. A. Marsh, H. McCallon, S. Schneider, R. Stiening, M. Sykes, M. Weinberg, W. A. Wheaton, S. Wheelock, and N. Zacarias. *2MASS All Sky Catalog of point sources.* (2003).

[58] R. J. Assef, C. S. Kochanek, M. Brodwin, R. Cool, W. Forman, A. H. Gonzalez, R. C. Hickox, C. Jones, E. Le Floc'h, J. Moustakas, S. S. Murray, and D. Stern. *Low-Resolution Spectral Templates for Active Galactic Nuclei and Galaxies from 0.03 to 30 μm*. ApJ**713**, 970 (2010). 0909.3849.

[59] L. M. Rebull, D. L. Padgett, C.-E. McCabe, L. A. Hillenbrand, K. R. Stapelfeldt, A. Noriega-Crespo, S. J. Carey, T. Brooke, T. Huard, S. Terebey, M. Audard, J.-L. Monin, M. Fukagawa, M. Güdel, G. R. Knapp, F. Menard, L. E. Allen, J. R. Angione, C. Baldovin-Saavedra, J. Bouvier, K. Briggs, C. Dougados, N. J. Evans, N. Flagey, S. Guieu, N. Grosso, A. M. Glauser, P. Harvey, D. Hines, W. B. Latter, S. L. Skinner, S. Strom, J. Tromp, and S. Wolf. *The Taurus Spitzer Survey: New Candidate Taurus Members Selected Using Sensitive Mid-Infrared Photometry*. ApJS**186**, 259 (2010). 0911.3176.

[60] S. M. Andrews, D. J. Wilner, C. Espaillat, A. M. Hughes, C. P. Dullemond, M. K. McClure, C. Qi, and J. M. Brown. *Resolved Images of Large Cavities in Protoplanetary Transition Disks*. ApJ**732**, 42 (2011). 1103.0284.

[61] A. Bayo, C. Rodrigo, D. Barrado Y Navascués, E. Solano, R. Gutiérrez, M. Morales-Calderón, and F. Allard. *VOSA: virtual observatory SED analyzer. An application to the Collinder 69 open cluster*. A&A**492**, 277 (2008). 0808.0270.

[62] J. Kauffmann, T. Pillai, and P. F. Goldsmith. *Low Virial Parameters in Molecular Clouds: Implications for High-mass Star Formation and Magnetic Fields*. ApJ**779**, 185 (2013). 1308.5679.

[63] F. Bertoldi and C. F. McKee. *Pressure-confined clumps in magnetized molecular clouds*. ApJ**395**, 140 (1992).